Hydrography of the Gulf of Mexico Using Autonomous Floats

PETER HAMILTON

Marine, Earth, and Atmospheric Sciences, North Carolina State University, Raleigh, North Carolina

ROBERT LEBEN

Colorado Center for Astrodynamics Research, University of Colorado Boulder, Boulder, Colorado

AMY BOWER AND HEATHER FUREY

Woods Hole Oceanographic Institution, Woods Hole, Massachusetts

PAULA PÉREZ-BRUNIUS

Centro de Investigación Científica y de Educación Superior de Ensenada, Ensenada, Mexico

(Manuscript received 3 October 2017, in final form 25 January 2018)

ABSTRACT

Fourteen autonomous profiling floats, equipped with CTDs, were deployed in the deep eastern and western basins of the Gulf of Mexico over a four-year interval (July 2011–August 2015), producing a total of 706 casts. This is the first time since the early 1970s that there has been a comprehensive survey of water masses in the deep basins of the Gulf, with better vertical resolution than available from older ship-based surveys. Seven floats had 14-day cycles with parking depths of 1500 m, and the other half from the U.S. Argo program had varying cycle times. Maps of characteristic water masses, including Subtropical Underwater, Antarctic Intermediate Water (AAIW), and North Atlantic Deep Water, showed gradients from east to west, consistent with their sources being within the Loop Current (LC) and the Yucatan Channel waters. Altimeter SSH was used to characterize profiles being in LC or LC eddy water or in cold eddies. The two-layer nature of the deep Gulf shows isotherms being deeper in the warm anticyclonic LC and LC eddies and shallower in the cold cyclones. Mixed layer depths have an average seasonal signal that shows maximum depths (~60 m) in January and a minimum in June–July (~20 m). Basin-mean steric heights from 0–50-m dynamic heights and altimeter SSH show a seasonal range of ~12 cm, with significant interannual variability. The translation of LC eddies across the western basin produces a region of low homogeneous potential vorticity centered over the deepest part of the western basin.

1. Introduction

Water masses in the Gulf of Mexico have sources in the Yucatan Current, which transports water from the Caribbean of differing characteristics into the basin through the Yucatan Channel (sill depth 2000 m). The Florida Straits has a sill depth of 800 m that limits the depth of the exit flow and thus upper-layer dynamics. The upper layer (above ~1000 m) of the Yucatan Current makes a clockwise loop in the Gulf [the Loop Current (LC)] and exits through the Florida Straits as the Florida Current and is thus a branch of the western boundary current. This upper-layer flow is the source of high-salinity Subtropical Underwater (SUW) and low-salinity Antarctic Intermediate Water (AAIW) brought into the basin from the Caribbean (Nowlin 1971, 1972). At irregular intervals between 4 and 18 months (Sturges and Leben 2000), the LC extends northward into the eastern Gulf and sheds a large (200–400-km diameter) anticyclone or ring (generally called an LC eddy) that translates westward or southwestward into the western basin, ultimately dissipating along the Mexican slope region (Fig. 1c). By these transport processes, upper-layer Caribbean water masses are brought into the interior of the Gulf where they are eventually transformed into Gulf Common Water (GCW; Nowlin 1971). Below ~1000 m, complex flows through the Yucatan

Corresponding author: Peter Hamilton, peter_hamilton@ncsu.edu

DOI: 10.1175/JPO-D-17-0205.1

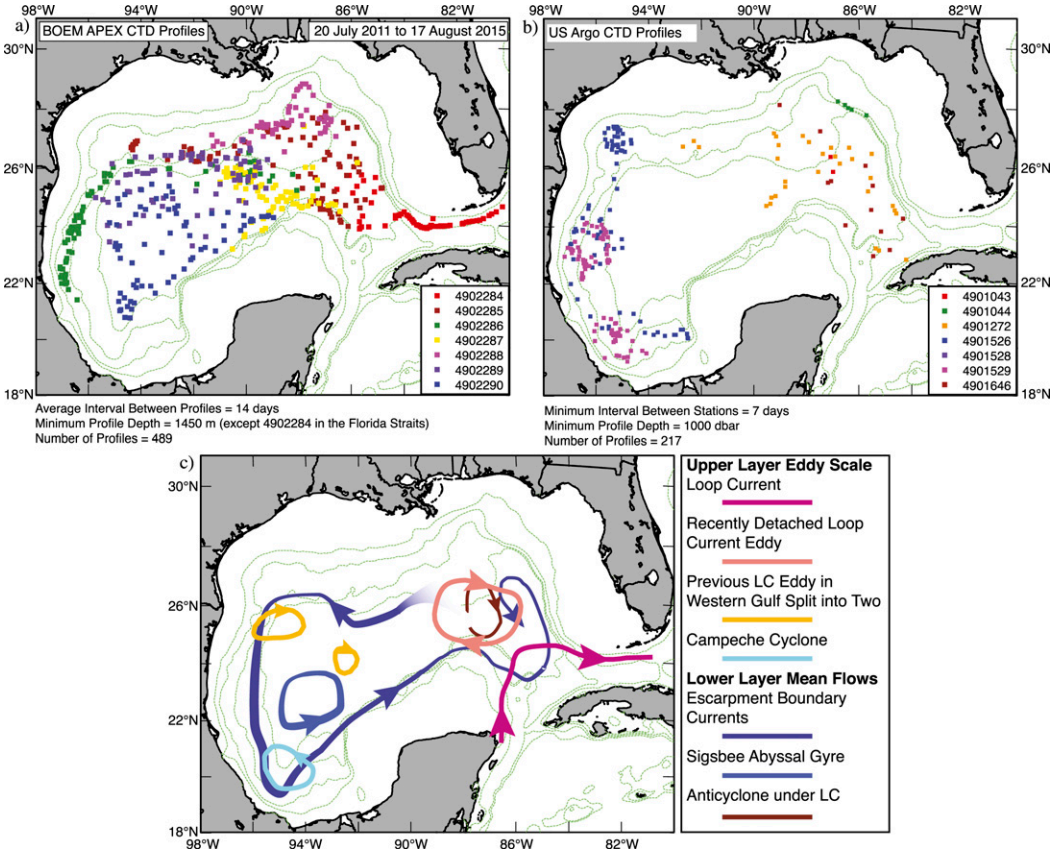

FIG. 1. Locations of CTD profiles for the indicated time interval for the indicated time interval from (a) this study and (b) the U.S. Argo archive, where locations are color coded by float number. (c) Sketch of upper- and lower-layer circulation features. Bathymetry contours for 100, 1000, 2000, and 3000 m.

Channel (Bunge et al. 2002; Candela et al. 2003) result in a net inflow of North Atlantic Deep Water (NADW) over the Yucatan Channel sill into the deep Gulf basin (Nowlin 1972; Sturges 2005).

Basinwide hydrographic surveys of the Gulf are extremely rare and are from pioneering studies from the 1930s to the 1970s that are reviewed and analyzed by Nowlin (1972). The early studies by Nowlin (1971) and Vidal et al. (1989) identified six and seven water masses, respectively, for the deep Gulf. Most of these are in the upper layer, have sources in the western Caribbean, and can be considered as components of GCW (e.g., 18°C Sargasso Seawater). Major sources, easily identified by temperature/salinity (T/S) characteristics, include SUW associated with the core of the western boundary current and AAIW, which originates in the South Atlantic as cold fresh dense water that sinks at the Antarctic Polar Front. The latter is found throughout the South Atlantic and tropical zones at ~700–1200 m (Nowlin 1972; Wust 1963).

Sturges (2005) studied the exchange of deep water from the Caribbean to the Gulf of Mexico in the depth range 800 to 1100 m, using the NODC hydrographic database. These depths are below the main LC flow and encompass both AAIW and upper NADW water masses. The main conclusion, based on the connection of potential vorticity (PV) contours for this layer between the Caribbean and the eastern Gulf, was that the mean flow was into the Gulf at these depths and, thus, the source of AAIW throughout the Gulf. In the Caribbean, AAIW minimum salinities could be influenced by waters from the South Atlantic through the Caribbean current and from the tropical North Atlantic through the Island Passages (e.g., the Windward Passage).

Below ~1000–1200 m, the Gulf is characterized by weak stratification and the relatively uniform composition of NADW. Below 1500 m (the lower depth limit in this analysis), historical deep profiles (from 1962) are given in Nowlin (1972) and show only slight decreases in potential temperature between 1500 and 3000 m of order 0.05°C.

More recently, Herring (2010) analyzed the available database of XBTs and CTDs from NODC and defined Gulf water in terms of combinations of water masses characterized by two standard profiles. The first contained high-salinity SUW that is related to the LC and

shed LC anticyclones, where the salinity maximum ~36.5–36.9 psu is found at ~100–150 m. The second is defined as GCW that is found outside of the LC and LC eddies, where the upper layers are cooler and fresher (Nowlin 1972). Herring (2010) used satellite altimetry derived sea surface height anomalies (SSHA) to estimate profiles as admixtures of the two characteristic mean profiles that corresponded to SSHA highs in the LC and LC eddies and to SSHA lows for GCW. Similar methods of deriving a subsurface density field have been used in numerical models of the Gulf that assimilate SSHA (Chassignet and Srinivasan 2015). Donohue et al. (2016b) show the locations of 1136 hydrocasts that extend below 1000 m in the historical record that they used to calibrate pressure-equipped inverted echo sounders (PIES) deployed in the Gulf (their Fig. A.1). Largest numbers are concentrated on the central northern slope and LC region. Coverage is sparse in the central and southern parts of the western basin. There are also surveys of localized features, usually LC eddies, such as those by Brooks and Legeckis (1982), Glenn and Ebbesmeyer (1993), Vidal et al. (1992), Cooper et al. (1990), and Vukovich and Waddell (1991). However, most of these later surveys had cast depth limits of ~700–800 m.

The deep basins of the Gulf can be considered a two-layer system based on velocity profiles that show coherent flows in the upper layer as energetic and strongly sheared and the lower layer as practically depth independent (Hamilton 2009; Hamilton et al. 2016a). The division between the upper and lower layers is well represented by the depth of the 6°C isotherm, which in the mean, is at approximately the depth of the Florida Straits sill (Bunge et al. 2002). Therefore, the great majority of upper-layer LC flows exit the Gulf through the Florida Straits above the depth of this isotherm.

The upper layer (0–~1000 m) dominated by the LC and LC eddies as well as secondary eddies that are primarily generated through interactions of the LC and LC eddies with slope topography and the existing eddy field. A ring in the western Gulf can be split into two by interactions with cyclones, where the cyclones are part of the surrounding eddy field (Biggs et al. 1996), or possibly generated by instabilities of the LC eddy itself (Hamilton et al. 2016b). Interactions of an LC eddy with the western slope produces companion cyclones, and resulting anticyclone–cyclone pairs often produce complex displacements toward and away from the western boundary slope as the eddies dissipate and mix with the surrounding Gulf water over intervals of several months (Vukovich and Waddell 1991). In the eastern basin, the LC often generates frontal cyclones through baroclinic instabilities (Donohue et al. 2016a; Hamilton et al. 2014) that interact with the slope regions to generate a range of eddy sizes of both rotations (Hamilton 2007a; Hamilton and Lee 2005; Hamilton et al. 2015).

The lower layer of NADW is dominated by topographic Rossby waves (TRW) (Hamilton 1990, 2009) and small-scale eddies. These deep currents are highly coherent and uniform with depth (below ~1000 m), and can be vigorous (Hamilton and Lugo-Fernandez 2001; Hamilton et al. 2016a). Generally, these lower-layer flows are not coherent with upper-layer eddy circulations. It is thought that LC and LC eddy interactions with deep topography generate westward-propagating TRWs (LaCasce 1998), though very recent observations with deep RAFOS floats indicate that larger-scale lower-layer eddies can coexist with transiting LC eddies in the western basin (Furey et al. 2017, manuscript submitted to *J. Phys. Oceanogr.*; Tenreiro et al. 2017). These recent observations of the deep circulation in the western basin, using 1500- and 2500-m isobaric RAFOS floats, indicate a narrow cyclonic boundary current along the steep escarpments from the northern slope (the Sigsbee and Perdido escarpments) around the western part of the Bay of Campeche, and continuing along the Campeche escarpment in the south (Fig. 1c). A cyclonic deep boundary current along the escarpments has been proposed by a number of authors (Chang and Oey 2011; DeHaan and Sturges 2005; Hamilton 2007b, 2009; Pérez-Brunius et al. 2018). A separate cyclonic gyre (known as the Sigsbee Abyssal Gyre; Fig. 1c; Pérez-Brunius et al. 2018) is also observed over the deepest part of the basin (Hamilton et al. 2016b; Pérez-Brunius et al. 2018).

Autonomous profiling floats have been used to map the salinity, temperature, and depth structures of the World Ocean since the turn of the century through the Argo program (Argo Science Team 1998; Roemmich et al. 2009). CTD profiles from Argo have been used to substantially increase the database for ocean heat content estimates with implications for climate change (Abraham et al. 2013). Recent studies include water-mass analysis (Billheimer and Talley 2016; Sato and Polito 2014), the vertical structure of eddies (Chaigneau et al. 2011), and basin-scale mean and annual cycles of steric height, salinity, and temperature (Roemmich and Gilson 2009), among many others. The Argo program specifically excluded marginal seas.

In this study, the hydrography of the Gulf of Mexico between July 2011 and August 2015 is addressed using CTD profiles collected by 14 Argo floats. Seven were autonomous profiling explorer (APEX) floats deployed as part of a larger program designed to map the deep circulation of the Gulf using RAFOS floats [funded by the Bureau of Ocean Energy Management (BOEM)]. Additional profiles from seven Argo floats, deployed in the Gulf by other programs and agencies, were obtained

from the Argo archive for the study period (July 2011–August 2015) so as to augment the database. A total of ~700 profiles were obtained in this four-year window, whereas in June 2016 there were 3759 operational floats in the World Ocean.

The seven BOEM APEX profiling floats were equipped with RAFOS acoustics and bio-optical sensors as well as a CTD (Seabird SBE41-CP). The bio-optical data are reported elsewhere (Green et al. 2014; Pasqueron de Fommervault et al. 2017). The RAFOS units were used to monitor the RAFOS sound sources as well as provide additional trajectory data at the parking depth of 1500 m, used for the majority of the RAFOS floats. Details of the complete study are given in Hamilton et al. (2016b). This paper focuses on the CTD data. Supplemental data in the form of altimeter-derived daily SSH maps on a 0.25° × 0.25° grid from CCAR (Leben 2005; Leben et al. 2002) and AVISO (Le Traon et al. 1998) are used in comparisons with CTD-derived dynamic heights.

The aims of this work are to map water-mass changes across the Gulf and investigate useful parameters such as mixed layer depths (MLDs) and depth of the 6°C isotherm (considered to be the division between upper and lower layers), their relationships to upper-layer cyclones and anticyclones, and the effectiveness of relating subsurface density fields to CCAR and AVISO SSH. In the following, section 2 discusses the databases and data processing, section 3 provides basic statistics, section 4 provides parameter analysis, section 5 discusses the seasonal cycle and the steric component of SSH, section 6 discusses the results, and section 7 is the summary.

2. Data

a. *APEX and Argo profiling floats*

The seven APEX floats deployed by the study were programmed to cycle to the surface from their nominal parking depth of 1500 m every 14 days. The CTD data were submitted to the Argo program (Roemmich et al. 2009) and underwent all their delayed-mode quality control (DMQC; Wong et al. 2015) procedures and corrections for drift before being included in the database. All the floats were equipped with the same SBE-41CP sensor from Sea-Bird Electronics, Inc., which has stated accuracies and stability for temperature of ±0.002°C and 0.0002°C yr^{-1}, respectively; and for salinity, accuracies are ±0.002 psu, with drift of 0.001 psu yr^{-1}, and corrected pressure accuracies are 2.4 dbar (Wong et al. 2015). Thus, instrumental error is expected to be minimal, and standard errors are caused primarily by mesoscale eddy variability. Deployments in different regions of the Gulf began in July 2011 (one float deployed) and continued in January 2012 (two floats), June–July 2012 (two floats), and September 2012 (two floats). The 1500-m parking depth is below the influence of upper-layer eddies. This reduces the likelihood of the floats leaving the Gulf via the Florida Straits or Yucatan Channel and also provides independent sampling of the upper-layer water column because flows of deep eddies and TRWs are not coherent with upper-layer eddies (Hamilton 2009). The Lagrangian integral time scale for deep water subinertial velocities, calculated from ~150 RAFOS float trajectories, ranges from about 3 to 10 days for different regions of the Gulf, with an overall average of ~5 days (Hamilton et al. 2016b). Therefore, it is assumed in the following analysis that the CTD profiles are independent samples. A total of 489 profiles were obtained that had cast depths greater than 1000 m, and their locations are shown in Fig. 1a. Note that profiles from float 4902284 that had cast depths less than 1000 m as it moved along the bottom of the Florida Straits are excluded from the profile counts, but are analyzed in Green et al. (2014) (Fig. 1a).

Apart from study-specific profiles, an additional seven U.S. Argo floats that were present in the Gulf during this same interval were obtained from the archive. The casts were filtered such that the minimum depth was 1000 m, the depth record was complete, and there were at least seven days between profiles. The resulting locations are given in Fig. 1b. All these latter floats had parking depths of ~1000 m and were deployed primarily to monitor the upper layer, often with cycle times of ~1–5 days and often with the purpose of assimilation into near-real-time models. Circulation at 1000 m could be influenced both by overlying eddies and deep TRW flows, but the seven-day interval should be adequate in most cases to decorrelate eddy circulations. A total of 217 locations were added to the database that provided increased coverage in the LC, along the western boundary, and in the Bay of Campeche (Fig. 1).

b. *Altimetry*

Gridded (0.25° × 0.25°) altimetry products are used to provide SSH from CCAR (Leben 2005; Leben et al. 2002) and AVISO. Satellite altimeters cannot directly measure absolute SSH because of imprecise knowledge of the marine geoid at length scales commensurate with the Gulf. Deriving SSH measurements from SSHA provided by the altimeters rely on estimates of the mean dynamic topography from a data assimilative model (Kantha et al. 2005; Leben et al. 2002) in the case of CCAR or from a variety of in situ and satellite measurements (Rio et al. 2010) in the AVISO product. There are also differences in the optimal interpolation schemes used to calculate gridded fields from along-track data. Altimeter data from a total of five operational satellites (*Jason-1*, *OSTM/Jason-2*, *Envisat*,

Cryosat-2, and *SARAL/AltiKa*) were available during the time period of the study, with ground track repeat intervals of 10, 17, and 35 days. The CCAR product is more tuned to the mesoscale eddy scales, whereas AVISO generally produces smoother daily fields particularly in the western Gulf.

Additionally, the AVISO product SSH (including the mean SSH) contains the seasonal steric signal, whereas in the CCAR product the steric SSH is effectively removed by high-pass filtering of the along-track data. To remove the steric signal, which has no dynamic significance, the daily basinwide mean, for bottom depths >200 m, was subtracted from the AVISO SSH. Comparison of the two SSH fields with the 1000–50-m geopotential, at the APEX profile locations and times, showed a small discrepancy in the means. Therefore, 3 cm was added to the steric-demeaned AVISO SSH, which makes the SSH statistics from both products comparable. Basinwide SSH means are likely to be influenced by the long-term variability of the LC intrusions and LC eddy shedding during the four years of the experiment. The Gulf steric signal is discussed in more detail in the following sections. Removal of the steric SSH allows the use of tracking contours [e.g., the 17-cm SSH contour that tracks the LC and LC eddy fronts (Leben 2005)] throughout the annual heating and cooling cycle. In the following sections, SSH from the gridded CCAR and AVISO fields is interpolated to the location and time of each CTD profile. SSH > 17 and < −10 cm are used to identify anticyclones and cyclones, respectively.

c. *RAFOS floats*

A recent comprehensive study deployed 121 isobaric RAFOS floats at 1500 m and 31 at 2500 m that were tracked over the same four-year period as the data collected from the autonomous profiling floats. RAFOS float positions were determined at eight-hour intervals, with good record lengths ranging from a few days to 730 days; producing194 float years of location and deep velocity data. Mean currents were analyzed by aggregating float velocities into 0.5° × 0.5° overlapping boxes, centered on a 0.25° × 0.25° grid. The degrees of freedom for mean velocity were established by determining the number of unique days sampled in each bin divided by the Lagrangian integral time scale (LaCasce 2008), which was estimated to be about five days for deep Gulf flows. Details of these calculations and results are given by Pérez-Brunius et al. (2018) and in the study report (Hamilton et al. 2016b). It is not the purpose of this paper to discuss details of the mean deep circulation measured by these floats, but rather to draw inferences for the hydrographic structures in the western Gulf (see section 6).

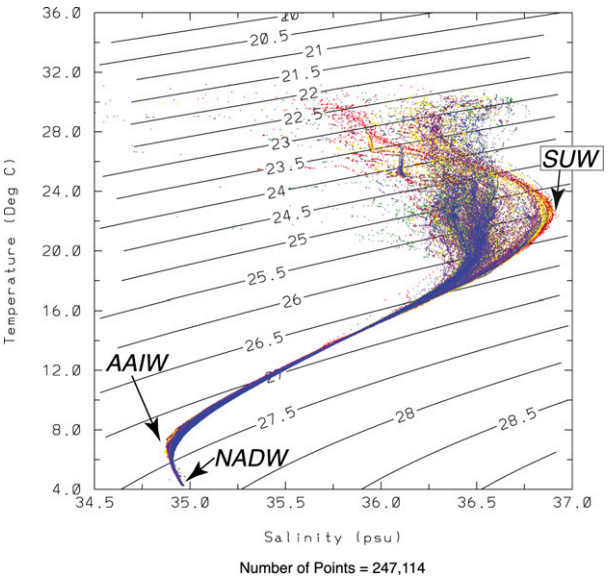

FIG. 2. *T*/*S* diagram for APEX CTD profiles. Locations given in Fig. 1a; color coded by float number (see Fig. 1a). Contours are of density (sigma-t; σ_t) in kg m^{-3}.

3. Basic statistics

The *T*/*S* diagram for all the 489 APEX profiles in Fig. 1a is shown in Fig. 2. Note the extremely tight *T*/*S* curve for temperatures less than 16°C that correspond to deep GCW. The separation of the upper layers into water masses containing SUW seems to be best divided by 36.6 psu. Traditionally 36.5 psu has been used (Nowlin 1972; Wust 1963), but with higher-resolution recent profiles 36.6 psu is a better divider. The salinity minimum for $\sigma_t \cong$ 27.3 kg m^{-3} corresponds to AAIW, and $\sigma_t >$ 27.5 kg m^{-3} identifies NADW. The upper layers are highly variable because of seasonal heating (generally restricted to the surface 50 m) and brackish inputs from the multitude of rivers, particularly from the northern Gulf (e.g., the Mississippi). The average temperature and salinity profiles, for all locations in Fig. 1, with standard deviations and extremes, as well as the subsets with SSH > 17 cm and SSH < −10 cm, using the CCAR data, are given in Fig. 3. Only small differences would be seen in the SSH-defined subsets if AVISO SSH were used. As expected, the mean profiles show a more prominent and deeper SUW salinity maximum, higher temperatures, and the AAIW salinity minimum at a deeper depth for anticyclones (SSH > 17 cm) compared with cyclones (SSH < −10 cm).

For each temperature, salinity, and depth profile from the APEX and U.S. Argo profiles, a set of characteristic parameters was derived as follows:

1) SSH: Interpolated to the location and time of the profile from daily CCAR and AVISO 0.25° altimeter maps.

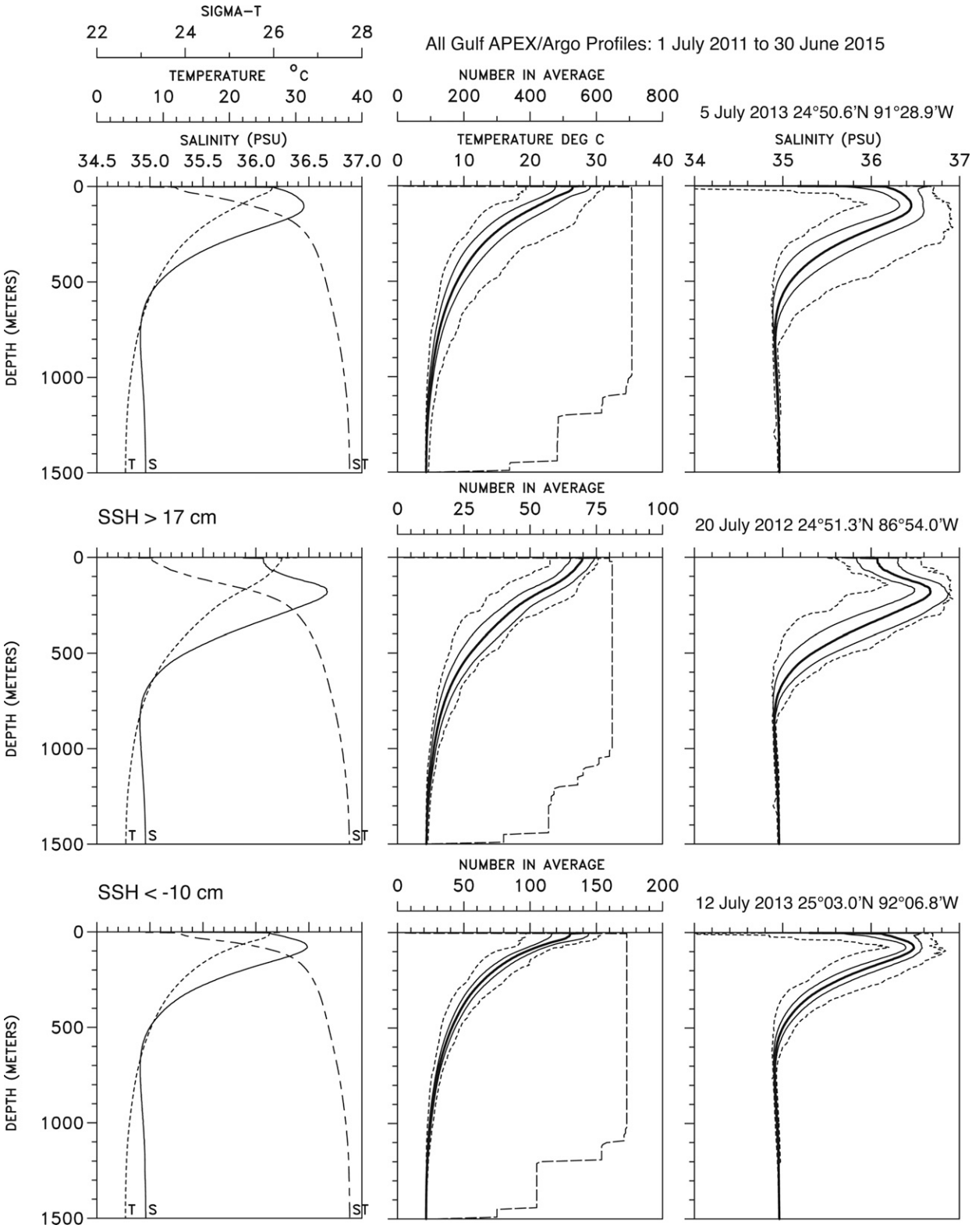

FIG. 3. Statistics from APEX/Argo CTD profiles. (left) Average profiles of T, S, and σ_t. (right) The means, standard deviations (thin solid lines), and extrema (thin dashed lines) for the temperature and salinity profiles. (center) The number of values at each depth is given by the long-dashed lines. (top) All available profiles, (middle) profiles filtered for CCAR SSH > 17 cm, and (bottom) SSH < -10 cm.

2) Depth of the 6°C isotherm: Interpolated using the profile depth and temperature data. The 6°C isotherm, derived from temperature–depth profiles, is a good indicator of the depth extent of the LC and LC eddies. Because the mean is also the depth of the Straits of Florida sill (Bunge et al. 2002), it may also be used as the division between upper and lower layers in the Gulf.
3) 1000–50-m dynamic height: A measure of the upper-layer geostrophic circulation that can be directly compared with SSH. The lower integration limit corresponds to the common deepest depth of the profiles and the approximate depth extent of the upper layer. The 50-m upper limit excludes seasonal heating and surface mixed layer effects.
4) Depth of the AAIW salinity minimum: The salinity minimum is searched for in the salinity–depth profile where $\sigma_t > 27.0$.
5) AAIW properties: Salinity, temperature, and σ_t at the depth of the salinity minimum.
6) NADW properties: Depth, potential temperature θ, and salinity of the potential density $\sigma_\theta = 27.715\,\mathrm{kg\,m^{-3}}$ surface. This has an average depth of 1283 m; well below the direct influence of upper-layer eddies. The very tight T/S relation for depths below 1000 m (Fig. 2) indicate that θ and S are uniquely defined for a given σ_θ, and any variability is likely to be within the accuracy of the measurements. Because this analysis uses a smaller set of profiles (those to ~1500 m), it will be given separately.
7) SUW depth and thickness: The salinity maximum is searched for the part of the σ_t profile between 24.5 and 26.5. If $S_{\max} > 36.6$ psu, the depth is computed, and the thickness is defined for the adjacent parts of the S profile where $S \geq 36.6$ psu.
8) SUW properties: Salinity, temperature, and σ_t at the salinity maximum if it exists.
9) Surface MLD: MLD is computed using the temperature and density profiles. The criteria developed by de Boyer Montegut et al. (2004) for individual profiles are applied. The temperature and density profiles are searched downward from the near-surface 10-m values until the differences are $|\Delta T| = 0.2$°C and $\Delta\sigma_\theta = 0.03\,\mathrm{kg\,m^{-3}}$. The MLD estimates from the two methods produce similar results for most profiles with the T criteria being slightly deeper.
10) Surface layer temperature and salinity: T and S are averaged from 0 to 10 m.

The statistics are calculated for these derived parameters, and averages and standard deviations are given in Table 1 for all profiles and separately for anticyclones (LC and LC eddies) and cyclones identified by locations where the criteria SSH > 17 cm and SSH < −10 cm are met, respectively, for both the CCAR and AVISO datasets. The overall average 6°C isotherm depth is 800 m, and about 100 m deeper and 50 m shallower in anticyclones and cyclones, respectively. These depths are about 50 m deeper than the AAIW salinity minima. In anticyclones, AAIW is slightly warmer and less dense, because of the stronger influence of LC source waters, and thus on SSH > 17 cm statistics. Average SSH and dynamic height show similar changes in magnitudes between the three cases, as would be expected if the SSH anomalies are tracking the highs and lows associated with mesoscale eddies. The mean SSH is close to zero for all stations, indicating that the coverage is not biased to any particular region of the Gulf. The differences between AVISO and CCAR statistics for cyclones and anticyclones are a reflection of the number of locations that are not common to both subsets (Table 1).

Similarly, SUW statistics (Table 2) are consistent with cyclones and anticyclones. Almost all the locations with SSH > 17 cm have traces of SUW with the salinity maximum at an average depth of 175 m. The maximum salinity found was 36.926 psu, and 83%/95% of the locations (75/73) with SUW present and CCAR/AVISO SSH >17 cm had salinity maxima >36.75 psu. Average thickness of water with $S > 36.6$ psu in anticyclones is ~100 m. MLDs have the same consistent relation to the mean of about 35 m, being deeper and shallower in anticyclones and cyclones, respectively. Mean 0–10-m surface layer salinity is 36.181 psu with a range from 32.574 to 36.708 psu.

In the lower layer, NADW statistics (Table 3) employ the deeper casts to 1500 m, which only use the BOEM study floats. For these calculations, the depth z of the 27.715 σ_θ level is found, followed by interpolation to estimate $T(z)$, $S(z)$, and $\sigma_\theta(z)$. If the calculated $\sigma(z)$ differs by more than 0.001 from 27.715, the cast is rejected. The 27.715 surface varies in depth by ~400 m, with almost no change in salinity. The variation in θ is within the margin of error. Table 3 also includes temperature statistics for the 1283-m depth level (the mean depth of the σ_θ surface). It is significant, however, that even at >1000 m, the upper layer influences the variation of depth of the density surfaces. Again, the surface is deeper (shallower) and the 1283-m temperature is warmer (cooler) than the mean for SSH > 17 (< −10 cm). Only the AVISO SSH are used because the AVISO data better correlates with deep isotherm depths (see section 4b).

4. Parameter analysis

a. Maps

The spatial distribution of parameters is estimated by averaging the parameters over grid boxes arranged to

TABLE 1. Statistics from APEX/Argo CTD profiles. Number of common locations for CCAR (C) and AVISO (A) SSH > 17 cm = 62 and for SSH < −10 cm = 131.

Type of profile (number)	Statistic	SSH (cm)	6°C isotherm depth (m)	50–1000-m dynamic height (10^{-1} J kg^{-1})	AAIW depth (m)	AAIW T (°C)	AAIW S (psu)	AAIW σ_t
All (704)	Ave	−0.75 (C); −0.55 (A)	800.12	108.47	745.34	6.354	34.902	27.429
	Std dev	15.18 (C); 16.80 (A)	68.41	16.07	80.66	0.246	0.010	0.038
CCAR SSH > 17 (81)	Ave	32.91	887.3	138.85	820.1	6.483	34.896	27.407
	Std dev	13.56	78.70	18.43	98.86	0.342	0.007	0.047
AVISO SSH > 17 (79)	Ave	36.72	915.6	143.27	851.8	6.442	34.898	27.414
	Std dev	13.33	61.55	14.54	85.99	0.343	0.008	0.047
CCAR SSH < −10 (172)	Ave	−14.97	746.4	95.99	691.3	6.348	34.904	27.432
	Std dev	4.00	42.13	5.92	57.72	0.227	0.012	0.037
AVISO SSH < −10 (230)	Ave	−15.62	740.1	95.03	680.7	6.379	34.903	27.426
	Std dev	4.30	37.42	4.75	52.91	0.236	0.011	0.038

cover most of the deep Gulf. This is generally preferable to averaging the T/S profiles in a grid box and then calculating the parameters from the averaged T/S profile (Lozier et al. 1994) because the latter will reduce extrema. Water masses that depend on defining extrema (e.g., AAIW or SUW) are better characterized from individual profiles. The adopted grid of 24 approximately square elements with a width of ~2° longitude is given in Fig. 4. The average density of stations within each grid square is ~27, with the lowest numbers of profiles (10) in boxes 12 and 22 and the highest number (67) in box 3. As a check on how well major features are represented by the space and time averaging, the CCAR and AVISO SSH from the profile locations and times, averaged over grid boxes, are compared with the four-year average of the daily SSH maps that are on a 0.25° grid. The comparison is given in Fig. 5, and despite the sparseness of profile grid data, and thus the subsampling of the SSH data, the major features of both mean SSH fields (e.g., the LC, and highs and lows in the western basin) are fairly well reproduced. Standard error (SE) of the subsampled AVISO and CCAR SSH averages 2.63 and 2.03 cm, respectively, and the distributions over the grid are shown as shaded contours in Figs. 5c,d. The SE patterns reflect both the degrees of freedom (e.g., higher in the central western Gulf) and regions of higher variability (e.g., the eastern edge of the LC). The distributions of SE are similar (except for magnitudes) for all other mapped parameters.

CCAR and AVISO four-year means from daily SSH differ with AVISO being smoother, particularly in the western Gulf, where an anticyclone dominates the deep part of the basin and a cyclone in the Bay of Campeche (the latter is present but less intense in the CCAR map; Fig. 5a), both associated with wind stress curl forcing (Sturges 1993; Vazquez de la Cerda et al. 2005). These 4-yr means (Figs. 5a,b) are very similar to the 20-yr (1993–2012) respective mean SSH surfaces that are given in Hamilton et al. (2016b). In the grid-averaged location SSH, the LC is prominent in the east (Figs. 5c,d), though much less intense with a relatively weaker intrusion in the AVISO map (Fig. 5d). The low–high–low triplet between 26°N and the Bay of Campeche along the western slope in the CCAR maps are reproduced, as well as the lows and highs in the center of the western basin (Figs. 5a,c). The latter are weaker and more

TABLE 2. SUW and MLD statistics from APEX/Argo CTD profiles.

Type of profile (number)	% of profiles with SUW	Statistic	SUW thickness (m)	SUW depth (m)	SUW T (°C)	SUW S (psu)	MLD from T (m)	MLD from density (m)
All (704)	37.5%	Ave	47.3	125.2	22.038	36.730	37.96	30.96
		Std dev	44.7	50.93	1.266	0.098	27.65	25.65
CCAR SSH > 17 (81)	92.6%	Ave	98.4	174.6	22.384	36.832	52.88	42.05
		Std dev	38.1	35.5	0.793	0.061	37.01	34.94
AVISO SSH > 17 (79)	92.4%	Ave	101.5	180.5	22.499	36.833	57.85	44.16
		Std dev	34.6	31.5	0.679	0.056	42.02	39.85
CCAR SSH < −10 (172)	15.7%	Ave					29.98	24.90
		Std dev					16.56	15.29
AVISO SSH < −10 (230)	20.4%	Ave					30.11	24.47
		Std dev					18.13	16.45

TABLE 3. NADW statistics for $\sigma_\theta = 27.715$ surface and temperature at 1283 m.

Number of locations	All locations (478)				AVISO SSH > 17 cm (55)		AVISO SSH < −10 cm (159)	
	Depth (m)	Θ (°C)	Salinity (psu)	T at 1283 m (°C)	Depth (m)	T at 1283 m (°C)	Depth (m)	T at 1283 m (°C)
Ave	1283.0	4.326	34.954	4.446	1366.0	4.581	1227.6	4.380
Std dev	70.2	0.012	0.002	0.092	64.3	0.119	50.9	0.043
Max	1495.8	4.350	34.958	4.867	1495.8	4.867	1383.6	4.522
Min	1086.2	4.291	34.949	4.265	1212.1	4.374	1111.9	4.265

broken up in the altimeter SSH map than on the profile grid, again a function of resolution. In the AVISO comparison for the western basin, the large anticyclone is more intense and displaced westward (Fig. 5d), but the distribution of highs and lows west of 92°W has strong similarities with the CCAR grid-averaged means, though the AVISO map (Fig. 5d) is less noisy (Figs. 5c,d). However, the Campeche Bay cyclone is only suggested in Figs. 5c,d, because of the low resolution of the ~2° grid (Fig. 4).

A measure of the differences between the 0.25° daily averaged, four-year mean SSH maps (Figs. 5a,b) and grid-averaged location fields (Figs. 5c,d) is constructed by subsampling the four-year mean field at the locations of the stations, averaging over each grid box and subtracting the grid-averaged field where the locations are time variable. This is denoted by <SSH> − SSH, where the angle brackets denote the daily averaged, four-year mean and are shown for CCAR and AVISO by shaded contours in Figs. 5a,b. Table 4 gives the statistics on the differences that show slightly better agreement between the CCAR maps than for AVISO, largely attributable to a better representation of the mean LC. The low magnitudes of the standard errors and SSH difference fields (Table 4 and Fig. 5) indicate that mapped parameters are reasonable representations of higher-resolution fields in the deep Gulf.

Mean maps of 1000–50-m dynamic height and the depth of the 6°C isotherm (Fig. 6) have similar features and the expected inverse relation. Besides the northward shoaling in the LC, there is a prominent high in the western basin and corresponding depression in the interface surface that also is similar to the AVISO SSH western high (Fig. 5d). The LC eddies that stall and slowly decay in the vicinity of the western boundary produce this western high in the dynamic height. The lesser similarity to the mean CCAR SSH (Fig. 5a) in the western Gulf is probably caused by a noisier mean surface there (see below).

The AAIW mean parameter maps are given in Fig. 7, and, as expected, the depth of the AAIW salinity minimum has the same pattern as the depth of the 6°C isotherm, but about 50 to 60 m shallower under the LC, which reduces to 20 to 30 m shallower in the west and in the Bay of Campeche. The salinity minimum shows a slow increase from east to west as the water mass becomes more distant from its input source in the Yucatan Channel (Fig. 7b). The density σ_t of the salinity minimum also increases from east to southwest corresponding to the increase in salinity and ~0.4°C decrease in temperature. It is noted that deep mixing can occur through the trapping of near-inertial waves in anticyclones that can extend down to the depths of the AAIW salinity minimum (Pallàs-Sanz et al. 2016). Colder deep temperatures in the southwest are influenced by the dynamic height low and the cyclonic gyre in the Bay of Campeche (Pérez-Brunius et al. 2013; Vazquez de la Cerda et al. 2005). The standard error pattern is shown for AAIW depth (Fig. 7a). For the other parameters, the patterns are similar, so the maps (Figs. 7b–d) just indicate the mean and range of SE to avoid clutter.

The SUW mean parameter maps are given in Fig. 8. The percentage of locations in each grid box that show presence of SUW ranges from >70% in the LC to 30%–40% across a swath of the central and western Gulf, to less than 10% in the northwest and southwest corners

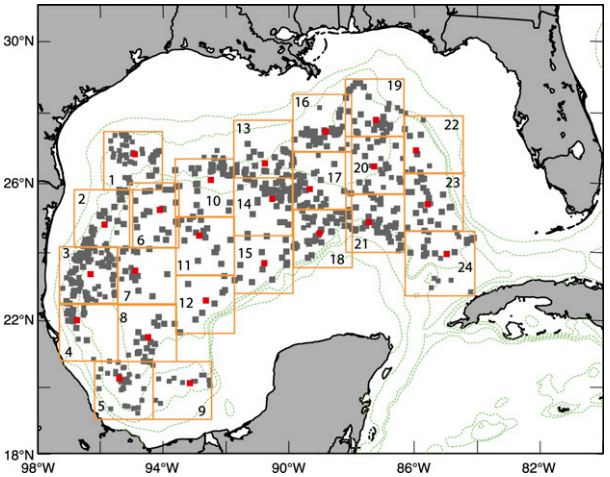

FIG. 4. Map of analysis grid squares, where CTD profile locations from APEX and U.S. Argo profiling floats are given by black squares. Numbered orange squares give grid-averaging boxes with the averaged locations within each box given by the red squares. The grid is used for contour maps of the box area averages of analysis parameters derived from individual T/S profiles.

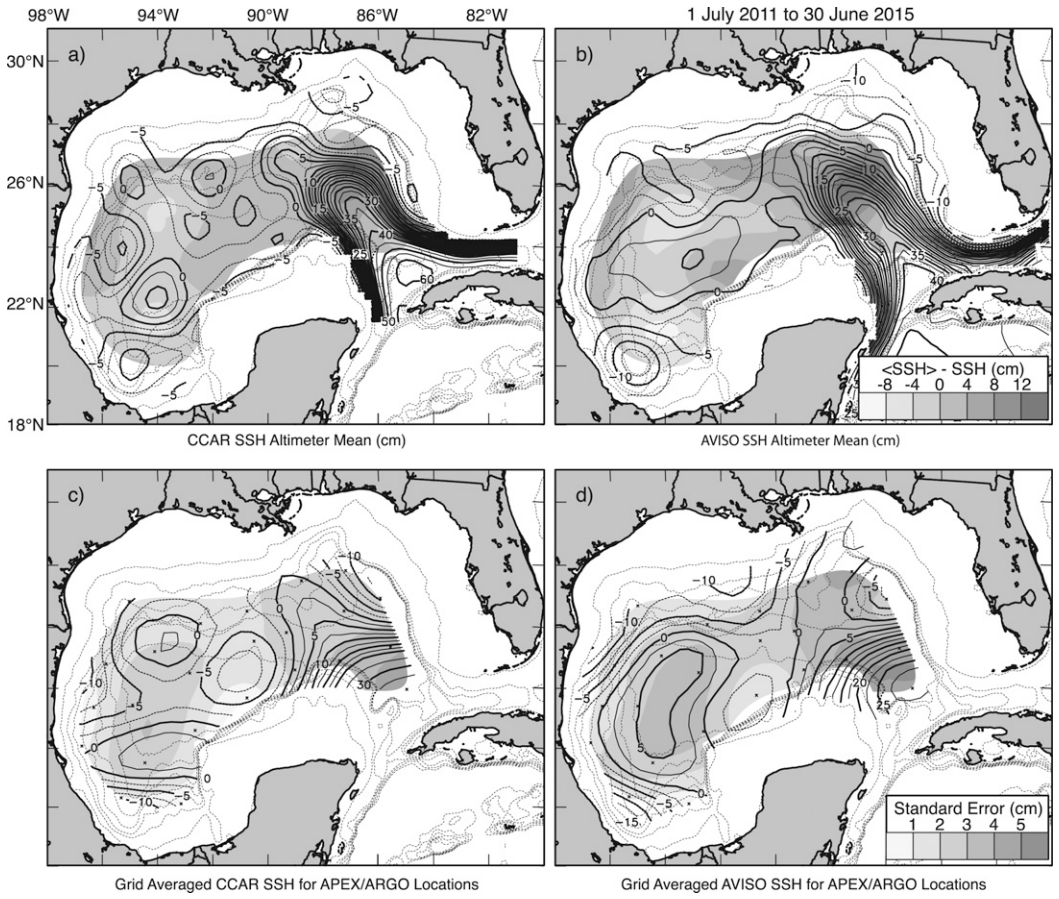

FIG. 5. (a) CCAR and (b) AVISO four-year mean SSH from daily 0.25° gridded altimeter SSH maps; (c) CCAR and (d) AVISO ~2° square grid-averaged SSH using APEX and Argo profile locations in Fig. 4, where shaded contours are of standard error. In (a) and (b) shaded contours show the differences between the four-year daily SSH altimeter mean <SSH> and the grid-averaged SSH in (c) and (d), respectively.

(Fig. 8d). The source of SUW is the Yucatan Current with the salinity maximum of the 70–90-m-thick core ($S > 36.6$ psu), at depths between 180 and 150 m (Figs. 8a,b). The SUW core thickness is at a maximum in the northeast from northward extensions of the LC and in the central western basin from the mean WSW trajectories of LC eddies (Elliott 1982; Hamilton et al. 1999; Vukovich and Crissman 1986). However, the SUW maximum salinity decreases from >36.8 psu in the LC to 36.65 psu on the western boundary (Fig. 8c), indicating a mixing of the core with surrounding Gulf common water.

Interestingly, the depth of this core deepens from where the SUW is thickest in the western basin (~92 to 94°W) toward the western boundary near 23°N (from ~130 to ~170 m; Figs. 8a,b). This western maximum depth region roughly corresponds to similar maximum depths of AAIW and the 6°C isotherm (Figs. 7a and 6b). This implies that SUW water sinks or mixes downward in the region where LC eddies stall and/or interact with the western boundary, and may imply a return flow at depth in the thermocline as compensation for the westward drift of LC eddies and possibly surface mean flows as suggested by Sturges and Bozec (2013).

In the lower layer, maps of NADW parameters, represented by the depth of the 27.715 σ_θ isopycnal and the temperature at the mean depth of the surface (1283 m) are given in Fig. 9. The average grid is slightly different because of the elimination of shallow (<1000 m) casts. Compared to Fig. 4, the deep grid eliminates the Bay of Campeche and the northeast corner (squares 5, 9, and 22; Fig. 4). The isopycnal surface has a shallow region in the east, just on the northern edge of the mean LC

TABLE 4. Difference statistics for <SSH> − SSH.

	AVISO		CCAR	
	Mean (cm)	Std dev	Mean (cm)	Std dev
<SSH> − SSH	1.45	5.39	1.15	3.75
|<SSH> − SSH|	4.48	3.33	2.69	2.85

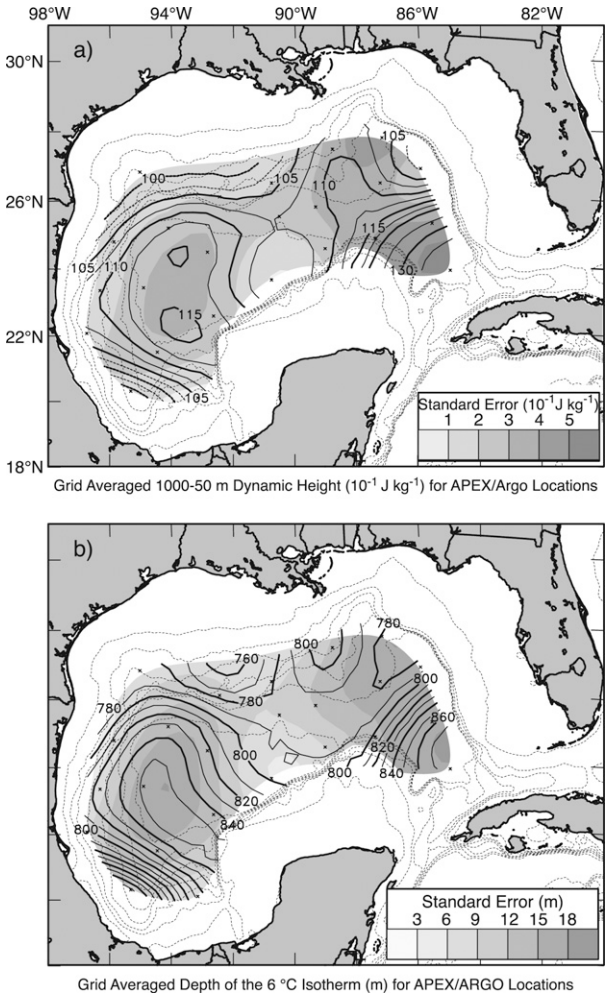

FIG. 6. (a) Dynamic height (10^{-1} J kg^{-1}) and (b) depth (m) of the 6°C isotherm from grid-averaged APEX and Argo profile locations in Fig. 4. Shaded contours show standard errors with the respective scales in the lower right-hand corner of the maps.

(Fig. 5), where isopycnals would slope up toward the surface. In the western basin, there is a depression of the surface in much the same region as the maxima in the 6°C isotherm and AAIW depths (Figs. 6b and 7a). Consequently, the eastern minimum and western maximum depths have cooler and warmer temperatures than the mean at 1283 m (Fig. 9b). The temperature map (Fig. 9b) also shows evidence of cooler water along the northern and western boundaries that lend support to DeHaan and Sturges's (2005) analysis that suggests a cyclonic boundary circulation in the western basin that gradually warms with distance from sources in the eastern Gulf (see section 6).

Deep currents from ~1000 m to the bottom are nearly depth independent (Hamilton 2009; Hamilton et al. 2016a) and generally uncorrelated with surface layer baroclinic flows. Thus, the depth of the effective interface between upper and lower layers is an important diagnostic for circulation dynamics. The recent RAFOS float study of the deep circulation in the Gulf indicates that the isobaric floats at a nominal 1500 m recorded small temperature changes along their tracks (Hamilton et al. 2016b). It would therefore be useful to be able to relate these changes to lower (or upper) layer thickness. The deepest practical level of temperature measurements from the APEX profiling floats was 1475 m, and the correlation of this temperature variability with the depth of the 6°C isotherm is shown in Fig. 9c. The scatterplot confirms that the depth of the interface between the upper and lower layers (i.e., the 6°C isotherm) can be inferred from in situ temperature at the depths of the floats with moderate skill. Potential vorticity constraints (LaCasce 2000) are likely to be a major control on deep currents. This topic will be explored in further studies of RAFOS float trajectories in the Gulf.

Mean surface-layer (0–10 m) salinities are given in Fig. 10 and show high values in the south-central part of the western basin, with lower values along the west Florida slope, off the Mississippi delta, and in the northwest corner. Mean surface-layer salinity for the deep basin is 36.18 with individual profiles in the range [36.71, 32.57]. The high surface salinity in the western basin is caused by a combination of LC eddies translating into this region and high evaporation rates in the summer. Lower salinities on the northern slope are likely to result from direct outflows of the Mississippi plume, which can be entrained into the LC and/or LC eddy fronts (Schiller et al. 2011), and indeed the lowest spot value (32.57 psu) was found on the slope just east of the delta (Fig. 10). However, Mississippi–Atchafalaya plumes also flow westward along the Louisiana and Texas coasts before being advected offshore where the Mexican shelf narrows (Cochrane and Kelly 1986). Counterrotating pairs of eddies against the Mexican slope ~26°N may produce offshore flows of less-saline shelf water (Vukovich and Waddell 1991). A small cluster of relatively low salinities are found in the spot values between 22° and 28°N against the Mexican–west Texas slope.

b. *Correlations*

The depth of the 6°C isotherm, hereafter denoted as d_6, is a good measure of the depth of the eddy-dominated upper layer as it corresponds to the thickness of the LC, and its average (800 m) is the bottom depth of the Florida Straits through which the LC exits the Gulf (Bunge et al. 2002). Because numerical modeling requires good estimates of the density structure, and at present, routine CTD sampling at sufficient spatial density is not available for the Gulf, the approach is

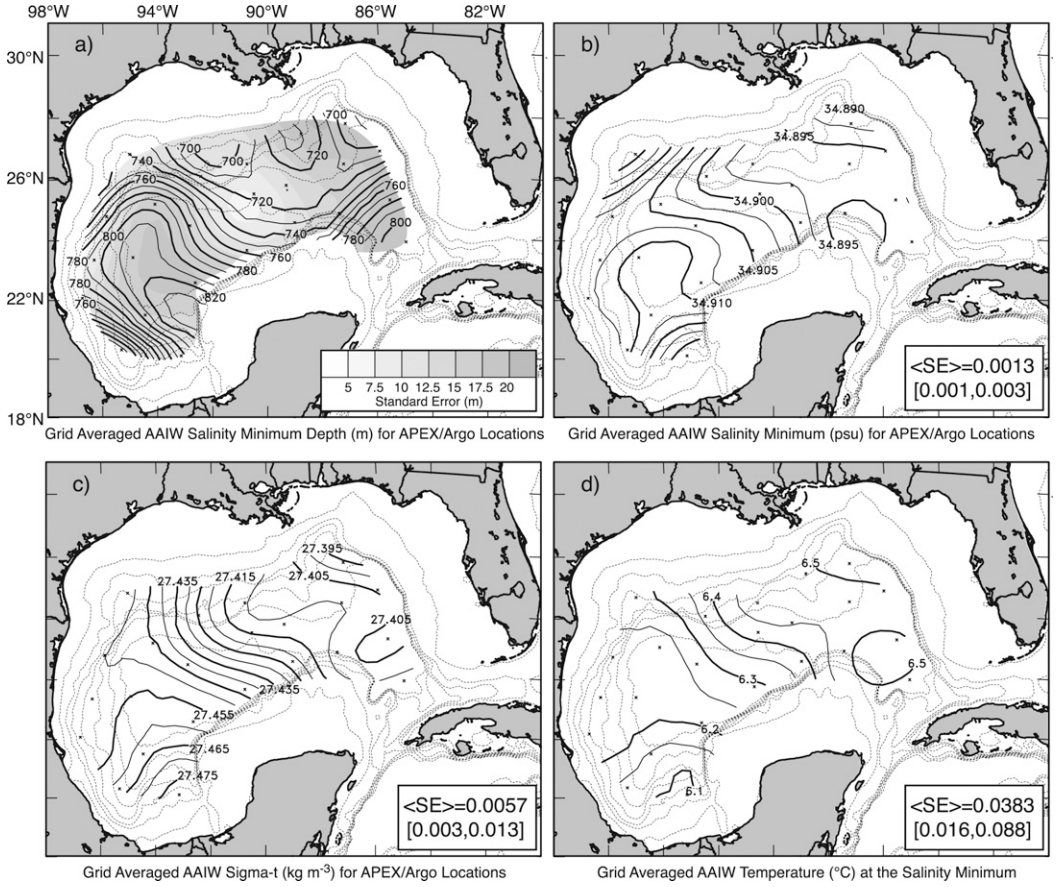

FIG. 7. Maps of AAIW mean parameters from grid-averaged APEX/Argo locations: (a) depth (m) of the salinity minimum, where the shaded contours give the standard error, (b) salinity minimum (psu), (c) density σ_t, and (d) temperature (°C) of the salinity minimum. Mean standard error <SE> and range of values are given in the lower right-hand corner of each plot.

to use altimeter SSHA as a proxy, with methods of varying sophistication. Essentially, assimilation relies on correlations of SSHA anomalies with the depth-dependent temperature and salinity structure, distinguishing profiles with SUW within the LC and LC eddies from the rest of the profiles with GCW (e.g., Herring 2010). The scatterplots of d_6 with 1000–50-m dynamic height and the CCAR and AVISO SSH are given in Fig. 11. It can be seen that there is scatter with d_6 versus dynamic height, with d_6 versus AVISO SSH having less scatter than d_6 versus CCAR SSH. Note that the steric signal in SSH is removed from these records by excluding the top 50 m from dynamic height and by the methods for SSH given in section 2. The scatterplots of CCAR and AVISO SSH against dynamic height, a more integrated measure of water column density variability, are given in Fig. 12, where again AVISO SSH has less scatter and a better slope than CCAR.

The histograms (Fig. 12b) show strong similarities between AVISO SSH and dynamic heights, whereas CCAR SSH has a peak between -5 and -10 (10^{-1} J kg^{-1}). There are relatively fewer numbers of CCAR SSH locations than for dynamic height and AVISO SSH below -10 (10^{-1} J kg^{-1}). This seems to be a result of the mean dynamic topography that is smoother for AVISO when compared to CCAR in the western basin. A comparison of the histograms for d_6 (Fig. 11b) and dynamic height (Fig. 12b) shows that the former has a broader distribution indicating that upper-layer depth and vertical density structure do not completely correspond. The correlations between the parameters are given in Table 5, which confirms that AVISO SSH correlates best with dynamic height, less so with d_6, and that CCAR SSH correlates with these variables less well.

5. Seasonal and steric variability

As an indication of the seasonal and interannual variability of the steric component of SSH in the Gulf, the daily deep-water average SSH signal that was

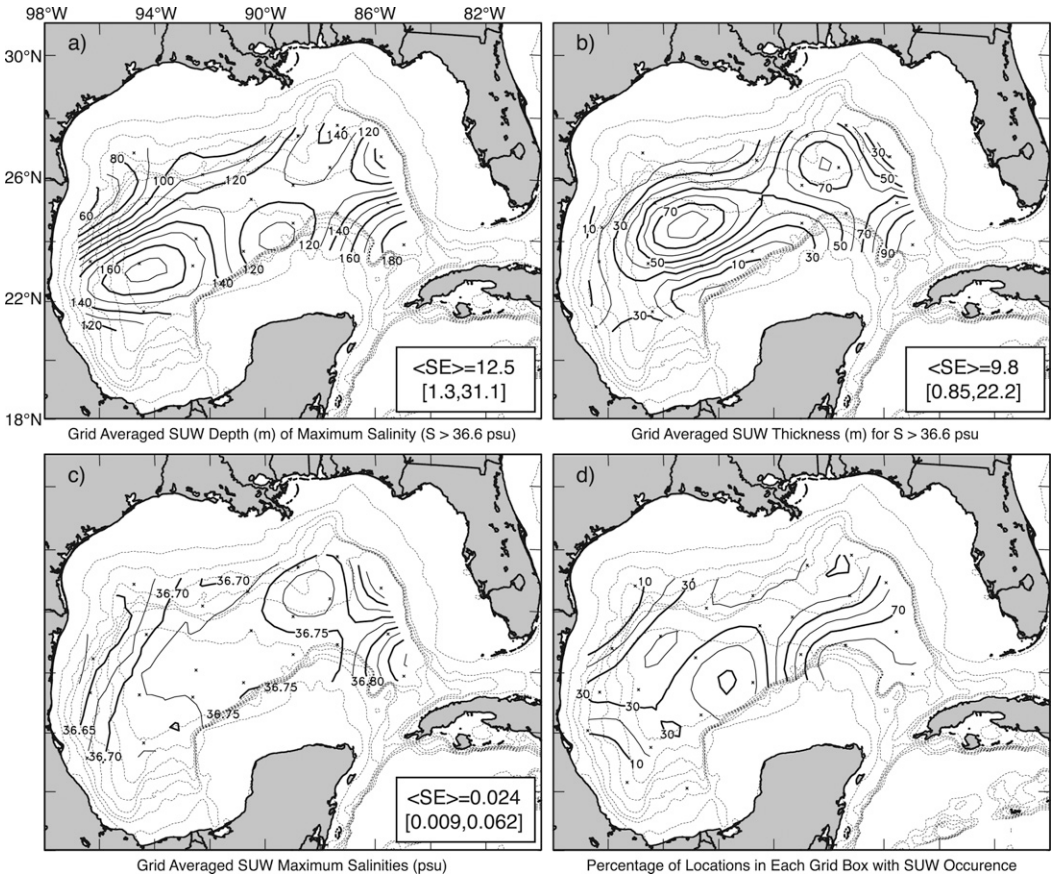

FIG. 8. Maps of SUW mean parameters from grid-averaged APEX/Argo locations: (a) depth (m) of the salinity maximum, (b) thickness for $S > 36.6$ psu, (c) salinity maximum, and (d) percentage of locations in each grid box with SUW present.

subtracted from the mapped AVISO product is given in Fig. 13. This is compared with the spatially averaged 0–50-m height equivalent [dynamic height divided by gravity (cm)] and the 0–10-m mean temperature, using all available profiling float locations in a given month. The monthly 0–50-m height equivalent represents the steric part of the signal that is excluded from the analyses in the previous sections. The steric SSH has summer–winter ranges of 10–20 cm over the four years with some interannual differences in summer maxima, winter minima, and the lengths of the summer and winter seasons. Comparisons are not precise because the varying number of profiling float stations are not necessarily evenly distributed over the Gulf on a monthly basis; however, the monthly height equivalent and temperature signals generally reflect the broad features of the daily steric height, though with smaller interannual differences.

The annual cycles of mixed layer depths from temperature and density are given in Fig. 14, where all the profiles that occur in a given month, irrespective of year, are averaged. The number of locations (degrees of freedom) ranges from a minimum of 50 in August to a maximum of 75 in October. As indicated in the statistics (Table 2), MLD from temperature is deeper than from density, though both follow the same cycle with maxima in December and January and minima in June and July. The surface (0–10 m) layer temperature and the steric equivalent height cycles show lags of 1–2 months with minima in February and March and maxima in August and September, resulting from the heat storage capacity of the upper layers of the Gulf.

Ocean heat content anomaly (HCA) is the deviation from the mean of upper-layer heat content (HC) (Willis et al. 2004), where

$$\mathrm{HC} = C_P \rho \int_0^h T\, dz \quad \text{and} \qquad (1)$$
$$\mathrm{HCA} = \mathrm{HC} - \mathrm{HC}_0,$$

where C_p is the heat capacity, ρ is a reference density, and h is the lower limit of integration. The HC_0 is the

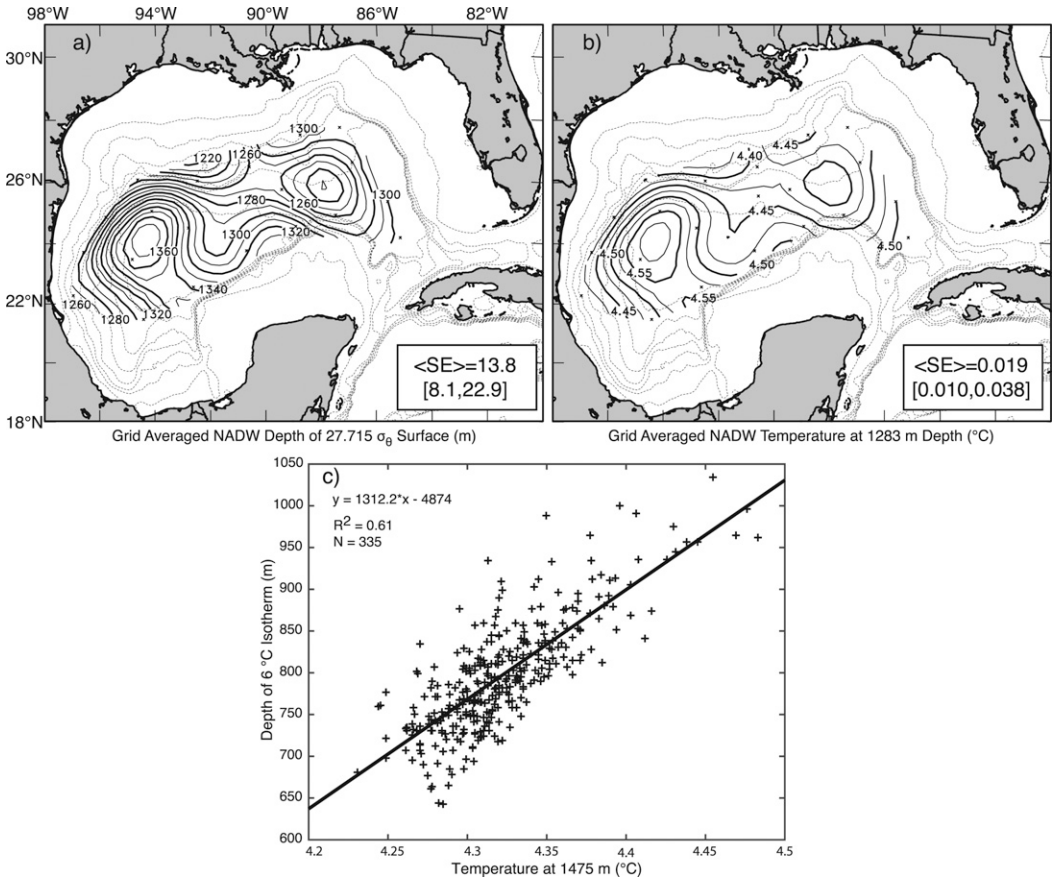

FIG. 9. Maps of NADW mean parameters from grid-averaged APEX/Argo locations: (a) depth (m) of the 27.715 σ_θ surface and (b) temperature (°C) at 1283 m. (c) Scatterplot of the depth of the 6°C surface vs temperature at 1475 m.

mean heat content of the upper layer, calculated from (1) using the mean $T(z)$ from Fig. 3. For $h = 800$ m, $HC_0 = 41.43 \times 10^9$ J m^{-2}. There is only a small difference between HC_0 and <HC> (<HC> $- HC_0 = 1.34 \times 10^9$ J m^{-2}); therefore, the preference is to use the mean $T(z)$ profile, because that would be generally used for estimating total HC. The lower depth limit of 800 m conforms to previous studies (Abraham et al. 2013; Willis et al. 2004) and also corresponds to the mean depth of the 6°C isotherm. For AVISO SSH > 17 and SSH < −10 cm, mean HCA = 9.56 ± 3.69 and HCA = −3.94 ± 1.70 (10^9 J m^{-2}), respectively, showing the increased heat content in the LC and LC anticyclones. Figure 14a includes the mean annual cycle of HCA (estimated in the same way as the annual cycle of MLD), which does not exactly mimic steric height but seems to be also influenced by MLD. The winter months (December–March) have relatively constant HCA, followed by a minimum in May, a month before the minimum MLD, and then a rapid rise to a peak in September. May to September also has a large increase in steric height. To the authors' knowledge, this is the first estimate of the annual cycle of heat content for the whole deep-water Gulf.

6. Discussion

In the eastern basin, the upper layer (0–~800 m) is dominated by the extensions of the LC and the western basin by the transits of shed LC eddies; both are warmer and saltier than the surrounding Gulf water. Figure 15 shows LC eddy life histories from separation from the LC to the last observed location during the four years of the study. Tracking was performed from the altimeter maps using the 17-cm SSH contour as given by Leben (2005) and Donohue et al. (2008). The timelines in Fig. 15 are split into the intervals between separation and the center crossing 90°W, from 90°W to the first encounter with the western slope (i.e., the transit time across the western basin), and the time to the last observation after encountering the western slope. The inset map shows the center tracks, which have a general WSW direction across the western basin that has been previously observed in many eddy-tracking studies (Donohue et al. 2008; Elliott

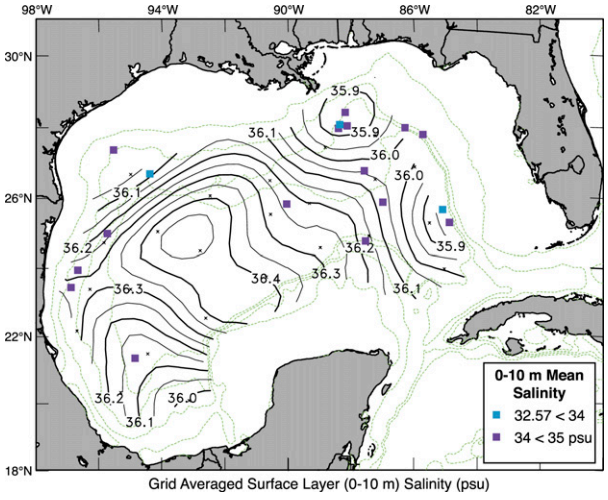

FIG. 10. Contours of grid-averaged surface layer (0–10 m) salinity (psu) with spot locations of individual profiles where surface 0–10-m mean salinities are less than 34 (blue) and 34 < 35 psu (magenta).

1982; Hamilton et al. 1999; Vukovich and Crissman 1986). There is considerable variability in both separation events and subsequent behavior of the LC eddies. The first two eddies (Hadal and Icarus) spent little time in the east before transiting the western basin, but the next two (Jumbo and Kraken) spent a few months in the east before crossing 90°W. Jumbo lived up to its name as a very large (~400-km diameter) eddy after separation, but it underwent complex interactions with the LC that caused it to split into two. The two parts subsequently merged into a smaller eddy after they followed separate paths through the relatively restricted region between the Mississippi delta and the Campeche Bank. The formation of Lazarus after the separation of Kraken (see LC area plot in Fig. 15) was slow, and the LC grew to one of the largest areal coverages ever observed, extending northwestward past the delta. A small Lazarus separated in July 2014 but was reabsorbed a month later by a still extending LC. There was another separation of a small anticyclone (named Michael), but that eddy rapidly dissipated. This very large, sustained LC extension really did not shed any significant eddies into the western basin, until the eventual separation of Nautilus in May 2015. A consequence is that there is a long ~15-month period, after the death of Kraken (March 2014), when there are no active LC eddies in the western basin. There is a

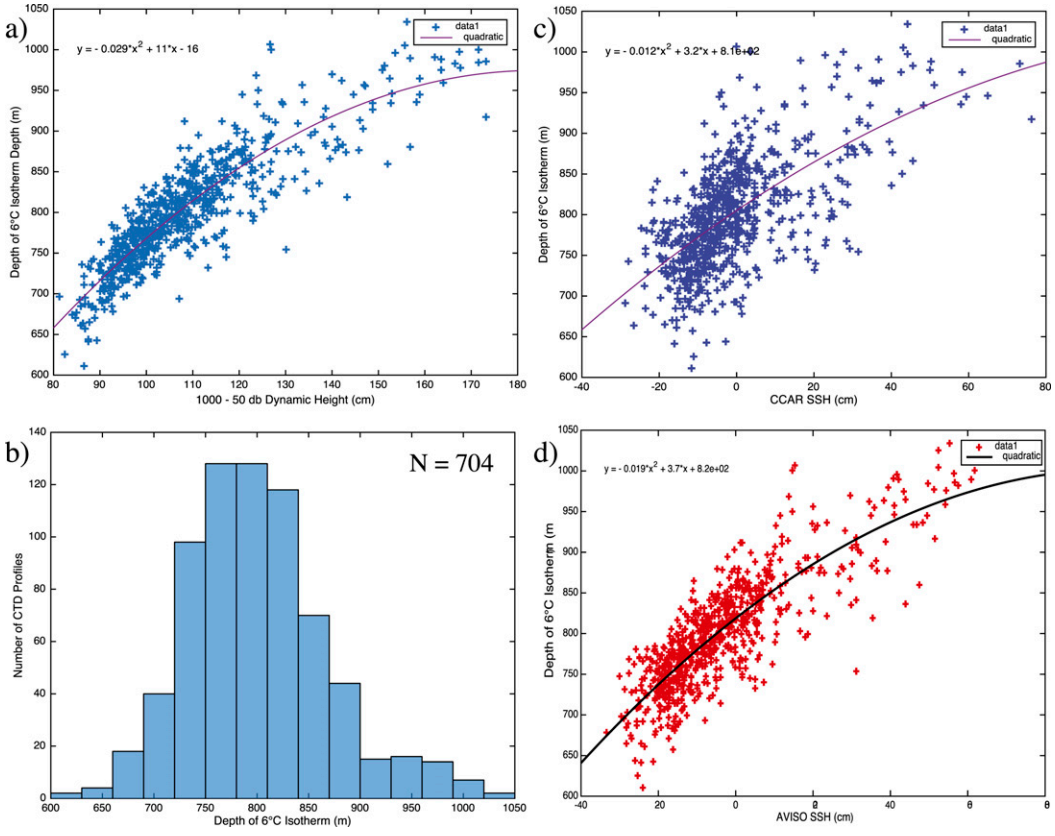

FIG. 11. Scatterplots of depth of 6°C isotherm derived from (a) APEX/Argo CTD profiles and dynamic height and with (c) CCAR and (d) AVISO SSH anomalies. (b) Histogram plot of the 6°C isotherm depth at the location and time of the profiles.

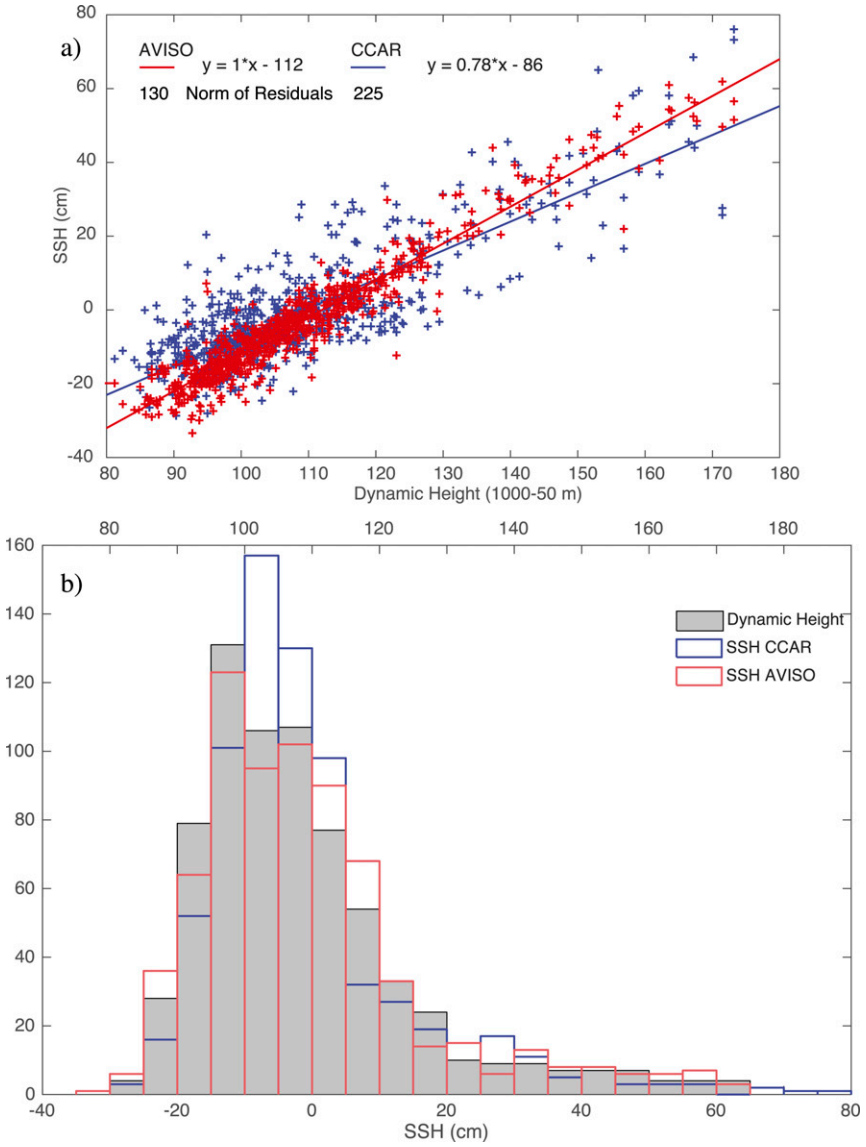

FIG. 12. (a) Scatterplots of AVISO and CCAR SSH against 1000–50-m dynamic height and (b) histogram plots of dynamic height and AVISO and CCAR SSH for the locations and times of the CTD profiles.

similar ~6-month period after the dissipation of Jumbo before Kraken crosses 90°W. Note that LC eddies can be split by interactions with cold cyclones in the western Gulf (Biggs et al. 1996), and this occurred for Hadal in the western part of the basin. More details on these eddies may be found in Hamilton et al. (2016b).

The inset map of Fig. 15 indicates that the western basin, because of LC eddy transits, on average, will have a warmer and deeper upper layer in east-northeast–west-southwest band across the region west of the delta. This is consistent with historical LC eddy tracks noted above and results in the average depth of the 6°C isotherm in Fig. 6b showing a depression in the south-central western Gulf. The thickness of the lower layer, here approximated as the distance from the 6°C isotherm to the bottom, likely imposes a strong PV constraint on the lower-layer mean circulation. DeHaan and Sturges (2005) suggest that the

TABLE 5. Correlations.

Variable 1	Variable 2	R^2 (N = 704)
AVISO SSH	Dynamic height	0.91
AVISO SSH	6°C isotherm depth	0.69
CCAR SSH	Dynamic height	0.69
CCAR SSH	6°C isotherm depth	0.42
AVISO SSH	CCAR SSH	0.73

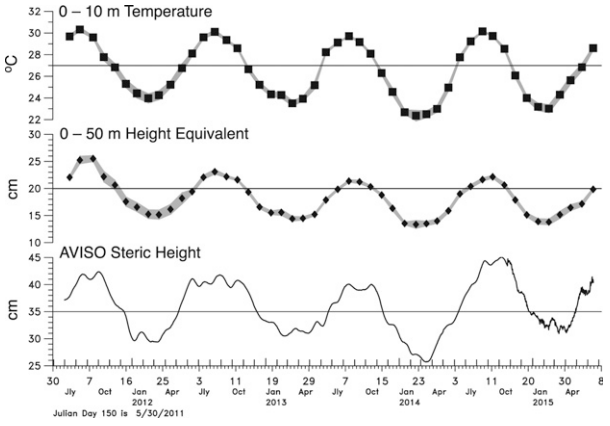

FIG. 13. (bottom) Daily AVISO SSH steric height signal removed from SSH maps for the time period of the observations; (middle) monthly 0–50-m height equivalent (dynamic height divided by g) averaged over all available APEX/Argo locations; (top) monthly 0–10-m mean temperature averaged over all available APEX/Argo locations. The gray bands show ± the standard error for each month.

deep circulation is cyclonic, and mooring and RAFOS float observations (Hamilton 2009) along the deep northern continental slope support the existence of a narrow westward flowing boundary current hugging the escarpments (the Sigsbee and Perdido escarpments).

The mean velocity (see section 2c) at 1500 m obtained from 161 RAFOS float tracks that were sampling the region in the same interval as the profiling floats analyzed here is shown in Fig. 16 (Hamilton et al. 2016b; Pérez-Brunius et al. 2018). The resulting mean flows confirm a deep cyclonic boundary current that continues from the northern escarpments southward along the deep Mexican slope, around the Bay of Campeche, and then eastward along the steep Campeche escarpment with some inflow into the eastern basin around the northern point of the Campeche Bank. Separate from this boundary current, there is a large-scale cyclonic gyre over the deepest part of the western basin. This gyre appears to be distinct from the deep boundary current, only connecting at the northeast corner of the Bay of Campeche (see deep mean circulation sketch in Fig. 1c). Further discussion of the deep gyre is given in Pérez-Brunius et al. (2018). Of interest here is the connection to the hydrography. Contours of the lower-layer PV, f/h_6, where h_6 is the thickness of the lower layer, are overlaid on the gridded mean currents in Fig. 16 and show that the gyre closely corresponds with the region of lowest PV that is also homogeneous within the resolution of the grid. PV contours based on total depth do not have the same correspondence with the cyclonic gyre. The region of nearly constant f/h_6 results from the shallow bowl-shaped bathymetry of the deepest part of the Gulf that almost exactly corresponds to the deepening of the mean deep temperature surfaces that are related to the cumulative LC eddy paths discussed above.

Though the cyclonic escarpment-hugging, deep boundary current has some explanation, ranging from rectification by TRW or eddy stresses (DeHaan and Sturges 2005; Hamilton 2009) to resulting from the large-scale response to LC intrusions (Chang and Oey 2011), the deep cyclonic gyre in the west has, as yet, no dynamical explanation. Speculations include accumulation and trapping of cyclonic vorticity generated as a deep response to the westward transit of LC eddies as seen in some numerical models (Welsh and Inoue 2000) and the maintenance of the gyre, which is only seen in the mean circulation and is not readily apparent in individual float trajectories, by deep eddy stresses (Pérez-Brunius et al. 2018).

7. Summary

Since the age of early Gulf of Mexico studies using ship-based hydrographic stations, a modern comprehensive survey of the water-mass structures using CTD-equipped autonomous profiling floats has been achieved. The early surveys (e.g., Nowlin 1972) were based on single basinwide cruises with widely spaced stations and limited vertical resolution. However, these pioneering surveys identified the principal water masses and their sources in the Yucatan Channel and the Caribbean. This study has sought to statistically examine the variability of these water masses across the basin and relate them to upper-layer LC and eddy activity. Additionally, the high-resolution CTD profiles allowed characterization of surface salinity, seasonal mixed layer depths, and upper-layer heat content. The results are relevant to defining density in numerical models of Gulf circulations and provide robust statistics (e.g., on the depth and distribution of AAIW, and seasonal mixed layer depths) not hitherto available for model validations, owing to the paucity and nonrandom nature of the existing databases.

Over a four-year interval, seven floats from this study and seven floats from U.S. Argo jointly collected 706 profiles to at least 1000 m (489 of these to 1500 m). Coverage was such that all parts of the deep basins could be statistically characterized over a relatively short period of time. Because the parking depth and time interval between casts of the floats (1500 m and 14 days for this study; 1000 m and at least 7 days for U.S. Argo), profiles are at essentially independent random locations; very few were entrained, while at their parking depths, by vigorous upper-layer eddy circulations common in the Gulf.

AVISO and CCAR altimeter-derived SSH were extracted for the locations and times of the profiles as

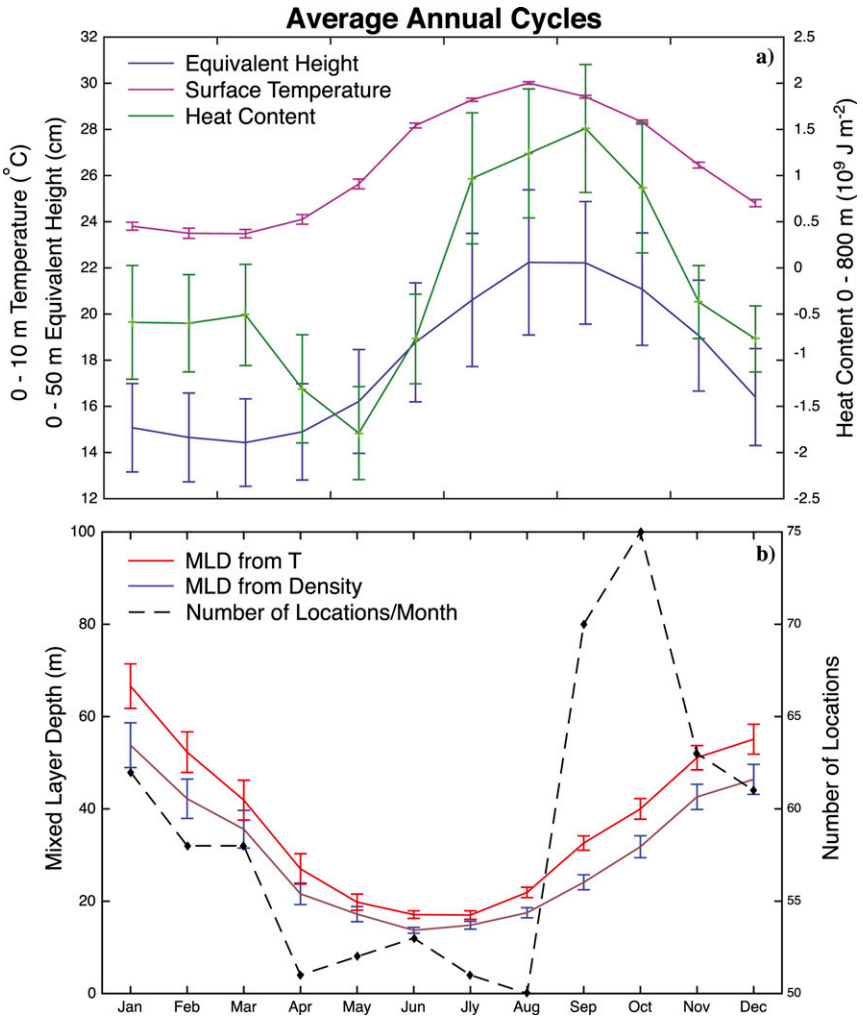

FIG. 14. Average annual cycle of monthly means from all locations of (a) 0–50-m equivalent height and 0–10-m surface temperature (left axis scale) and heat content anomaly (right axis scale) and (b) mixed layer depths from temperature and density. (bottom) The number of profile locations in each calendar month during the four-year study. The bars are standard errors.

complementary data to indicate whether the casts were taken in the LC or LC eddies (SSH $>$ 17 cm) or in cold cyclones (SSH $<$ -10 cm). Mean T, S, and σ_t profiles for SSH $>$ 17 cm have warmer and less dense upper-layer water with SUW (salinities $>$ 36.6 psu) present at ~150-m depth when compared to the average profiles using all casts. For SSH $<$ -10 cm, the characteristics are reversed with a colder more dense upper layer and salinities $<$ 36.5 psu. Below 800–1000 m, stratification is small, corresponding to the observations of near-depth independence of lower-layer currents (Hamilton 1990, 2009). Similarly, statistics of water-mass parameters (e.g., AAIW, NADW, 6°C isotherm, MLD) showed generally deeper (shallower) depths than average for anticyclonic (cyclonic) structures, a reflection of the two-layer nature of the deep basins of the Gulf. Similarly, deep density and temperatures, well below LC and LC eddy flows (at 1475 m), can be related to the thickness of the upper layer (i.e., the depth of the 6°C isotherm; Fig. 9c), even though the TRW and eddy dynamics of the lower layer are not usually correlated to the upper levels (Hamilton 2009; Hamilton et al. 2016a). At the locations and times of the profiles, AVISO SSH more highly correlates with 1000–50-m dynamic height and 6°C isotherm depths than the CCAR product. Differences between the CCAR and AVISO maps are attributed to differing mean surfaces and processing methods.

Steric height derived from 0–50-m dynamic height, averaged over all casts, showed a strong seasonal cycle that closely tracked the monthly mean surface

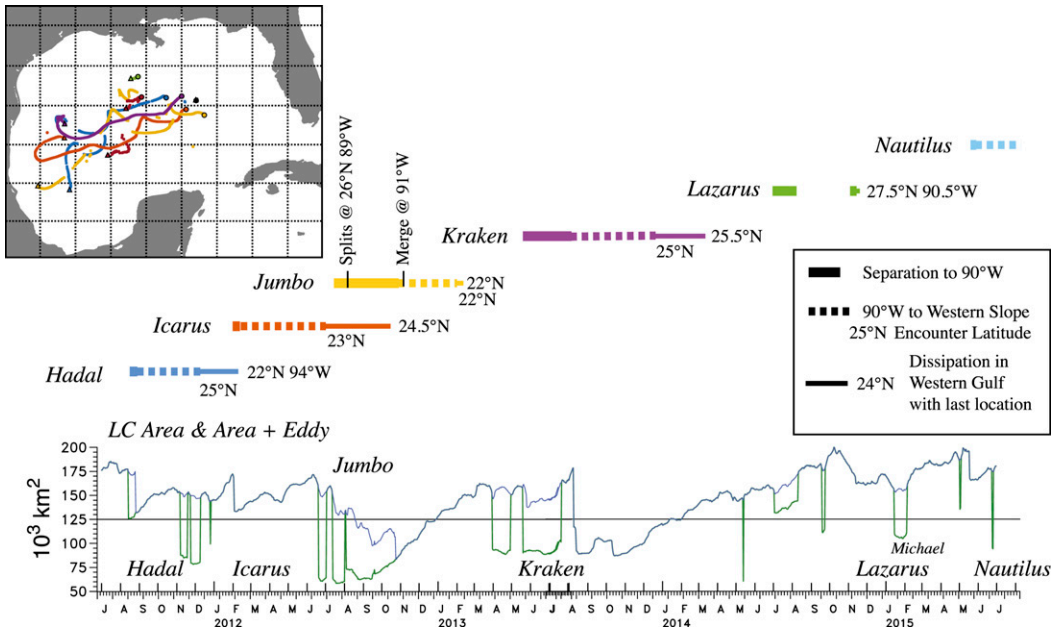

FIG. 15. Timeline of major LC eddy events in the Gulf of Mexico for the indicated interval. (bottom) The area of the LC (green line) and the area of the LC plus detached eddy (blue line) from the 17-cm (CCAR) SSH contour before it completely crosses a line from the delta to the northeast Yucatan. Legend gives the key to the time lines in different phases of the named eddy's life history. If the longitude is not given for the last location, then the location is against the western slope. In the western basin, AVISO 17-cm SSH contour is used. The inset map shows the tracks of the eddy centers from times of separation (filled circles) to the last identified eddy center location (filled triangles). Tracks and timelines are color coded by eddy names.

temperature with maxima and minima in August–September and February–March, respectively. Daily steric height from AVISO altimeter maps has significant interannual variability over the four years of observations. This signal needs to be removed from altimeter SSH maps so that consistent measures (e.g., the 17-cm SSH contour for the LC and major LC eddies) can be used from month to month (Leben 2005). The annual cycle of MLD is opposite to steric height (maximum in December; minimum in June–July) with about a two-month lead, an offset consistent with the heat storage capacity of the Gulf. The heat content annual cycle appears to be influenced by both the MLD and steric height cycles, producing a minimum and maximum in May and September, respectively, and only small changes during the winter (December–March).

Maps of water-mass distribution (SUW, AAIW) showed weak dispersion toward the west, consistent with the sources being within LC and Yucatan Channel waters. Traces of SUW are found all the way to the western slope, having been transported by westward-transiting LC eddies. Transits of LC eddies across the western basin have an influence on the mean deep isotherm surfaces, with the consequence of reducing the thickness of the lower layer above the deepest part of the western Gulf. This region of low PV coincides with a cyclonic gyre in the mean lower-layer currents that is centered over the deepest part of the western basin. The dynamics of this gyre are at present uncertain.

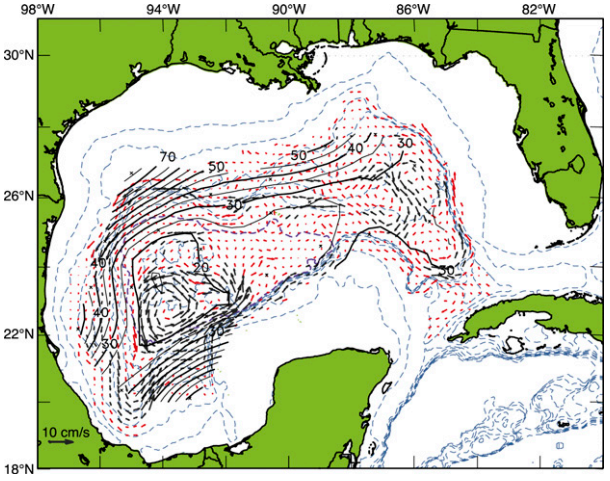

FIG. 16. Contoured lower-layer potential vorticity f/h_6 ($\times 10^9\,m^{-1}\,s^{-1}$), where h_6 is grid-averaged water depth–depth of 6°C isotherm, overlaid on mean velocity vectors derived from deep RAFOS floats, where black (red) arrows indicate averages significantly (not) different from zero at the 95% confidence level. For the PV calculations, bottom depths, latitude, and depth of the 6°C isotherm are grid averaged using the locations of the profiles. Dashed bathymetry contours are 100, 1000, 2000, 2500, 3000, 3250, 3500 (emphasized), and 3750 m (adapted from Hamilton et al. 2016a).

Acknowledgments. The authors were supported by the Department of the Interior, Bureau of Ocean Energy Management (BOEM), Contract M08PC20043 to Leidos, Inc., Raleigh, North Carolina. The authors also wish to acknowledge the enthusiastic support of Dr. Alexis Lugo-Fernández, the BOEM Contracting Officer's Technical Representative, during the study into the deep circulation of the Gulf of Mexico, using Lagrangian methods. Further support for the principal author was also provided through the Gulf Research Program of the National Academy of Sciences through a sub-award from Florida State University. The authors also gratefully acknowledge the assistance of Ms. Terry McKee of WHOI for managing the collection and organization of the BOEM APEX float data. BOEM and Argo profile data used in this study are available from the international and U.S. programs (https://doi.org/10.17882/42182).

REFERENCES

Abraham, J. P., and Coauthors, 2013: A review of global ocean temperature observations: Implications for ocean heat content estimates and climate change. *Rev. Geophys.*, **51**, 450–483, https://doi.org/10.1002/rog.20022.

Argo Science Team, 1998: On the design and implementation of Argo: An initial plan for a global array of profiling floats. CLIVAR Rep. 21., 32 pp.

Biggs, D. C., G. S. Fargion, P. Hamilton, and R. R. Leben, 1996: Cleavage of a Gulf of Mexico Loop Current eddy by a deep water cyclone. *J. Geophys. Res.*, **101**, 20 629–20 641, https://doi.org/10.1029/96JC01078.

Billheimer, S., and L. D. Talley, 2016: Annual cycle and destruction of Eighteen Degree Water. *J. Geophys. Res. Oceans*, **121**, 6604–6617, https://doi.org/10.1002/2016JC011799.

Brooks, D. A., and R. V. Legeckis, 1982: A ship and satellite view of hydrographic features in the western Gulf of Mexico. *J. Geophys. Res.*, **87**, 4195–4206, https://doi.org/10.1029/JC087iC06p04195.

Bunge, L., J. Ochoa, A. Badan, J. Candela, and J. Sheinbaum, 2002: Deep flows in the Yucatan Channel and their relation to changes in the Loop Current extension. *J. Geophys. Res.*, **107**, 3233, https://doi.org/10.1029/2001JC001256.

Candela, J., S. Tanahara, M. Crepon, B. Barnier, and J. Sheinbaum, 2003: Yucatan Channel flow: Observations versus CLIPPER ATL6 and MERCATOR PAM models. *J. Geophys. Res.*, **108**, 3385, https://doi.org/10.1029/2003JC001961.

Chaigneau, A., M. Le Texier, G. Eldin, C. Grados, and O. Pizarro, 2011: Vertical structure of mesoscale eddies in the eastern South Pacific Ocean: A composite analysis from altimetry and Argo profiling floats. *J. Geophys. Res.*, **116**, C11025, https://doi.org/10.1029/2011JC007134.

Chang, Y. L., and L. Y. Oey, 2011: Loop Current cycle: Coupled response of the Loop Current with deep flows. *J. Phys. Oceanogr.*, **41**, 458–471, https://doi.org/10.1175/2010JPO4479.1.

Chassignet, E. P., and A. Srinivasan, 2015: Data assimilative hindcast for the Gulf of Mexico. U.S. Dept. of Interior Bureau of Ocean Energy Management OCS Study BOEM 2015-035, 46 pp.

Cochrane, J. D., and F. J. Kelly, 1986: Low-frequency circulation on the Texas-Louisiana continental shelf. *J. Geophys. Res.*, **91**, 10 645–10 659, https://doi.org/10.1029/JC091iC09p10645.

Cooper, C. K., G. Z. Forristall, and T. M. Joyce, 1990: Velocity and hydrographic structure of two Gulf of Mexico warm-core rings. *J. Geophys. Res.*, **95**, 1663–1680, https://doi.org/10.1029/JC095iC02p01663.

de Boyer Montegut, C., G. Madec, A. S. Fischer, A. Lazar, and D. Iudicone, 2004: Mixed layer depth over the global ocean: An examination of profile data and a profile-based climatology. *J. Geophys. Res.*, **109**, C12003, https://doi.org/10.1029/2004JC002378.

DeHaan, C. J., and W. Sturges, 2005: Deep cyclonic circulation in the Gulf of Mexico. *J. Phys. Oceanogr.*, **35**, 1801–1812, https://doi.org/10.1175/JPO2790.1.

Donohue, K. A., P. Hamilton, R. R. Leben, D. R. Watts, and E. Waddell, 2008: Survey of deepwater currents in the northwestern Gulf of Mexico. U.S. Dept. of the Interior Minerals Management Service OCS Study MMS 2008-031, 375 pp.

——, D. R. Watts, P. Hamilton, R. Leben, and M. Kennelly, 2016a: Loop Current eddy formation and baroclinic instability. *Dyn. Atmos. Oceans*, **76**, 195–216, https://doi.org/10.1016/j.dynatmoce.2016.01.004.

——, ——, ——, ——, ——, and A. Lugo-Fernández, 2016b: Gulf of Mexico Loop Current path variability. *Dyn. Atmos. Oceans*, **76**, 174–194, https://doi.org/10.1016/j.dynatmoce.2015.12.003.

Elliott, B. A., 1982: Anticyclonic rings in the Gulf of Mexico. *J. Phys. Oceanogr.*, **12**, 1292–1309, https://doi.org/10.1175/1520-0485(1982)012<1292:ARITGO>2.0.CO;2.

Glenn, S. M., and C. C. Ebbesmeyer, 1993: Drifting buoy observations of a Loop Current anticyclonic eddy. *J. Geophys. Res.*, **98**, 20 105–20 119, https://doi.org/10.1029/93JC02078.

Green, R. E., A. S. Bower, and A. Lugo-Fernández, 2014: First autonomous bio-optical profiling float in the Gulf of Mexico reveals dynamic biogeochemistry in deep waters. *PLoS One*, **9**, e101658, https://doi.org/10.1371/journal.pone.0101658.

Hamilton, P., 1990: Deep currents in the Gulf of Mexico. *J. Phys. Oceanogr.*, **20**, 1087–1104, https://doi.org/10.1175/1520-0485(1990)020<1087:DCITGO>2.0.CO;2.

——, 2007a: Eddy statistics from Lagrangian drifters and hydrography for the northern Gulf of Mexico slope. *J. Geophys. Res.*, **112**, C09002, https://doi.org/10.1029/2006JC003988.

——, 2007b: Deep-current variability near the Sigsbee Escarpment in the Gulf of Mexico. *J. Phys. Oceanogr.*, **37**, 708–726, https://doi.org/10.1175/JPO2998.1.

——, 2009: Topographic Rossby waves in the Gulf of Mexico. *Prog. Oceanogr.*, **82**, 1–31, https://doi.org/10.1016/j.pocean.2009.04.019.

——, and A. Lugo-Fernandez, 2001: Observations of high speed deep currents in the northern Gulf of Mexico. *Geophys. Res. Lett.*, **28**, 2867–2870, https://doi.org/10.1029/2001GL013039.

——, and T. N. Lee, 2005: Eddies and jets over the slope of the northeast Gulf of Mexico. *Circulation in the Gulf of Mexico: Observations and Models, Geophys. Monogr.*, Vol. 161, Amer. Geophys. Union, 123–142.

——, G. S. Fargion, and D. C. Biggs, 1999: Loop Current eddy paths in the western Gulf of Mexico. *J. Phys. Oceanogr.*, **29**, 1180–1207, https://doi.org/10.1175/1520-0485(1999)029<1180:LCEPIT>2.0.CO;2.

——, K. Donohue, C. Hall, R. R. Leben, H. Quian, J. Sheinbaum, and D. R. Watts, 2014: Observations and dynamics of the Loop Current. U.S. Dept. of the Interior Bureau of Ocean Energy Management OCS Study BOEM 2015-006, 417 pp.

——, K. Speer, R. Snyder, N. Wienders, and R. R. Leben, 2015: Shelf break exchange events near the De Soto Canyon. *Cont. Shelf Res.*, **110**, 25–38, https://doi.org/10.1016/j.csr.2015.09.021.

——, A. Lugo-Fernández, and J. Sheinbaum, 2016a: A Loop Current experiment: Field and remote measurements. *Dyn. Atmos. Oceans*, **76**, 156–173, https://doi.org/10.1016/j.dynatmoce.2016.01.005.

——, A. S. Bower, H. Furey, R. Leben, and P. Perez-Brunius, 2016b: Deep circulation in the Gulf of Mexico: A Lagrangian study. U.S. Dept. of the Interior Bureau of Ocean Energy Management OCS Study BOEM 2016-081, 289 pp.

Herring, H. J., 2010: Gulf of Mexico hydrographic climatology and method of synthesizing subsurface profiles from the satellite sea surface height anomaly. Dynalysis of Princeton Rep. 122, 63 pp., http://gcoos.org/products/data/ssha/ssha_ts_proflies.pdf.

Kantha, L., J.-K. Choi, K. J. Schaudt, and C. K. Cooper, 2005: A regional data-assimilative model for operational use in the Gulf of Mexico. *Circulation in the Gulf of Mexico: Observations and Models, Geophys. Monogr.*, Vol. 161, Amer. Geophys. Union, 165–180.

LaCasce, J. H., 1998: A geostrophic vortex over a slope. *J. Phys. Oceanogr.*, **28**, 2362–2381, https://doi.org/10.1175/1520-0485(1998)028<2362:AGVOAS>2.0.CO;2.

——, 2000: Floats and *f*/*H*. *J. Mar. Res.*, **58**, 61–95, https://doi.org/10.1357/002224000321511205.

——, 2008: Statistics from Lagrangian observations. *Prog. Oceanogr.*, **77**, 1–29, https://doi.org/10.1016/j.pocean.2008.02.002.

Leben, R. R., 2005: Altimeter-derived Loop Current metrics. *Circulation in the Gulf of Mexico: Observations and Models, Geophys. Monogr.*, Vol. 161, Amer. Geophys. Union, 181–201.

——, G. H. Born, and B. R. Engebreth, 2002: Operational altimeter data processing for mesoscale monitoring. *Mar. Geod.*, **25**, 3–18, https://doi.org/10.1080/014904102753516697.

Le Traon, P. Y., F. Nadal, and N. Ducert, 1998: An improved mapping method of multisatellite altimeter data. *J. Atmos. Oceanic Technol.*, **15**, 522–533, https://doi.org/10.1175/1520-0426(1998)015<0522:AIMMOM>2.0.CO;2.

Lozier, M. S., M. S. McCartney, and W. B. Owens, 1994: Anomalous anomalies in averaged hydrographic data. *J. Phys. Oceanogr.*, **24**, 2624–2638, https://doi.org/10.1175/1520-0485(1994)024<2624:AAIAHD>2.0.CO;2.

Nowlin, W. D., Jr., 1971: Water masses and general circulation of Gulf of Mexico. *Oceanol. Int.*, **6**, 28–33.

——, 1972: Winter circulation patterns and property distributions. *Contributions on the Physical Oceanography of the Gulf of Mexico*, L. R. A. Capurro and J. L. Reid, Eds., Gulf Publishing Co., 3–51.

Pallàs-Sanz, E., J. Candela, J. Sheinbaum, J. Ochoa, and J. Jouanno, 2016: Trapping of the near-inertial wave wakes of two consecutive hurricanes in the Loop Current. *J. Geophys. Res. Oceans*, **121**, 7431–7454, https://doi.org/10.1002/2015JC011592.

Pasqueron de Fommervault, O., P. Pérez-Brunius, P. Damien, and J. Sheinbaum, 2017: Temporal variability of chlorophyll distribution in the Gulf of Mexico: Bio-optical data from profiling floats. *Biogeosciences*, **14**, 5647–5662, https://doi.org/10.5194/bg-14-5647-2017.

Pérez-Brunius, P., P. García-Carrillo, J. Dubranna, J. Sheinbaum, and J. Candela, 2013: Direct observations of the upper layer circulation in the southern Gulf of Mexico. *Deep-Sea Res.*, **85**, 182–194, https://doi.org/10.1016/j.dsr2.2012.07.020.

——, H. Furey, A. Bower, P. Hamilton, J. Candela, P. García-Carrillo, and R. Leben, 2018: Dominant circulation patterns of the deep Gulf of Mexico. *J. Phys. Oceanogr.*, **48**, 511–529, https://doi.org/10.1175/JPO-D-17-0140.1.

Rio, M. H., S. Mulet, P. Schaeffer, E. Greiner, and G. Larnical, 2010: Validation of the preliminary GOCE level-2 products. *Proc. Ocean Surface Topography Science Team Meeting*, Lisbon, Portugal, CNES, https://www.aviso.altimetry.fr/fileadmin/documents/OSTST/2010/oral/19_Tuesday/Rio.pdf.

Roemmich, D., and J. Gilson, 2009: The 2004–2008 mean and annual cycle of temperature, salinity, and steric height in the global ocean from the Argo Program. *Prog. Oceanogr.*, **82**, 81–100, https://doi.org/10.1016/j.pocean.2009.03.004.

——, and Coauthors, 2009: The Argo Program: Observing the global ocean with profiling floats. *Oceanography*, **22**, 34–43, https://doi.org/10.5670/oceanog.2009.36.

Sato, O. T., and P. S. Polito, 2014: Observation of South Atlantic subtropical mode waters with Argo profiling float data. *J. Geophys. Res. Oceans*, **119**, 2860–2881, https://doi.org/10.1002/2013JC009438.

Schiller, R. V., V. H. Kourafalou, P. J. Hogan, and N. D. Walker, 2011: The dynamics of the Mississippi River plume: Impact of topography, wind and offshore forcing on the fate of plume waters. *J. Geophys. Res.*, **116**, C06029, https://doi.org/10.1029/2010JC006883.

Sturges, W., 1993: The annual cycle of the western boundary current in the Gulf of Mexico. *J. Geophys. Res.*, **98**, 18 053–18 068, https://doi.org/10.1029/93JC01730.

——, 2005: Deep-water exchange between the Atlantic, Caribbean, and Gulf of Mexico. *Circulation in the Gulf of Mexico: Observations and Models, Geophys. Monogr.*, Vol. 161, Amer. Geophys. Union, 263–278.

——, and R. Leben, 2000: Frequency of ring separations from the Loop Current in the Gulf of Mexico: A revised estimate. *J. Phys. Oceanogr.*, **30**, 1814–1819, https://doi.org/10.1175/1520-0485(2000)030<1814:FORSFT>2.0.CO;2.

——, and A. Bozec, 2013: A puzzling disagreement between observations and numerical models in the central Gulf of Mexico. *J. Phys. Oceanogr.*, **43**, 2673–2681, https://doi.org/10.1175/JPO-D-13-081.1.

Tenreiro, M., J. Candela, E. Pallàs-Sanz, J. Sheinbaum, and J. Ochoa, 2017: Near surface and deep circulation coupling in the western Gulf of Mexico. *J. Phys. Oceanogr.*, **48**, 145–161, https://doi.org/10.1175/JPO-D-17-0018.1.

Vazquez de la Cerda, A. M., R. O. Reid, S. F. DiMarco, and A. E. Jochens, 2005: Bay of Campeche circulation: An update. *Circulation in the Gulf of Mexico: Observations and Models. Geophys. Monogr.*, Vol. 161, Amer. Geophys. Union, 279–293.

Vidal, V. M. V., F. V. Vidal, and J. M. Pérez-Molero, 1989: *Atlas Oceanografico del Golfo de Mexico*. Vol. I. Instituto de Investigaciones Electricas, 415 pp.

——, ——, and ——, 1992: Collision of a Loop Current anticyclonic ring against the continental slope of the western Gulf of Mexico. *J. Geophys. Res.*, **97**, 2155–2172, https://doi.org/10.1029/91JC00486.

Vukovich, F. M., and B. W. Crissman, 1986: Aspects of warm rings in the Gulf of Mexico. *J. Geophys. Res.*, **91**, 2645–2660, https://doi.org/10.1029/JC091iC02p02645.

——, and E. Waddell, 1991: Interaction of a warm ring with the western slope in the Gulf of Mexico. *J. Phys. Oceanogr.*, **21**, 1062–1074, https://doi.org/10.1175/1520-0485(1991)021<1062:IOAWRW>2.0.CO;2.

Welsh, S. E., and M. Inoue, 2000: Loop Current rings and deep circulation in the Gulf of Mexico. *J. Geophys. Res.*, **105**, 16 951–16 959, https://doi.org/10.1029/2000JC900054.

Willis, J. K., D. Roemmich, and B. Cornuelle, 2004: Interannual variability in upper ocean heat content, temperature and thermosteric expansion on global scales. *J. Geophys. Res.*, **109**, C12036, https://doi.org/10.1029/2003JC002260.

Wong, A., and Coauthors, 2015: Argo quality control manual for CTD and trajectory data. IFREMER Rep., 56 pp., https://doi.org/10.13155/33951.

Wust, G., 1963: On the stratification and circulation in the cold water sphere of the Antillean-Caribbean basins. *Deep-Sea Res.*, **10**, 165–187.